

# Environmental Science Advances

Accepted Manuscript

This article can be cited before page numbers have been issued, to do this please use: A. Loyola, R. Farajzadeh, D. Voskov, K. de Borst and S. Geiger, *Environ. Sci.: Adv.*, 2026, DOI: 10.1039/D6VA00162A.



This is an Accepted Manuscript, which has been through the Royal Society of Chemistry peer review process and has been accepted for publication.

Accepted Manuscripts are published online shortly after acceptance, before technical editing, formatting and proof reading. Using this free service, authors can make their results available to the community, in citable form, before we publish the edited article. We will replace this Accepted Manuscript with the edited and formatted Advance Article as soon as it is available.

You can find more information about Accepted Manuscripts in the [Information for Authors](#).

Please note that technical editing may introduce minor changes to the text and/or graphics, which may alter content. The journal's standard [Terms & Conditions](#) and the [Ethical guidelines](#) still apply. In no event shall the Royal Society of Chemistry be held responsible for any errors or omissions in this Accepted Manuscript or any consequences arising from the use of any information it contains.

Hundreds of depleted North Sea gas fields could enable Underground Hydrogen Storage (UHS) to support the decarbonization of energy and feedstock industries. For UHS to be viable, operations must ensure high purity and minimal hydrogen loss. This requires suitable site selection and optimal development planning, both of which are influenced by geology. Through numerical simulations of an ensemble of geological models of the Bunter Sandstone, this work identifies which operational strategies most affect UHS performance and how they interact with geological heterogeneities. Informed by these simulations, we propose a framework for screening sites and guiding development planning across geological scenarios. Notably, screening relies on a novel, quick-to-calculate metric, the gravity-purity number, which incorporates both geological and operational criteria.

View Article Online

DOI: 10.1039/D6VA00162A



# Evaluation of operational strategies for underground hydrogen storage in depleted gas fields under diverse geological scenarios: Guidelines for site screening and development planning

Ana Loyola<sup>\*1,3</sup>, Denis Voskov<sup>1</sup>, Rouhi Farajzadeh<sup>1,2</sup>, Karin de Borst<sup>2</sup>, and Sebastian Geiger<sup>1</sup>

<sup>1</sup>Faculty of Civil Engineering and Geosciences, Delft University of Technology, Delft, The Netherlands

<sup>2</sup>Shell Global Solutions International B.V., The Hague, The Netherlands

<sup>3</sup>Navier, ENPC, Institut Polytechnique de Paris, Univ Gustave Eiffel, CNRS, Marne-la-Vallée, France

## Abstract

Underground hydrogen storage in depleted gas fields is a potential solution for large-scale, seasonal storage of hydrogen, in support of the decarbonization of energy systems and other industrial activities. Its viability depends on the performance of the storage operations, which is influenced by the interaction between reservoir geology and operational strategies. However, general guidelines for development planning that account for geological uncertainty are still lacking. In addition, existing site screening criteria remain limited in that they do not account for how operational decisions can alter the suitability of a reservoir geology for hydrogen storage. Here, we employ a numerical model of flow and transport to evaluate a set of operational strategies in varying geological scenarios for depleted methane gas reservoirs of the Bunter Sandstone, an important formation in the North Sea. We investigate the following strategies for their impact on performance and interaction with geological features that are common in the Bunter sandstone: depletion level, injected hydrogen mass, cushion gas, well perforation, idle period, production rates, and methane reinjection. We found that depletion level, injected mass, and well perforation interact strongly with geology and are critical for site selection. The methane reinjection strategy provides pressure support that increases hydrogen production, though at the cost of purity in the long-term. Furthermore, cushion gas strategies show significant optimization potential but limited interaction with geology, whereas the duration of the idle period and target rates have low optimization potential. Based on these findings, we propose a site selection and development planning framework for underground hydrogen storage in depleted gas fields. The site selection phase introduces a novel screening criterion, the gravity–purity number, which integrates geological and operational considerations. The

\*Corresponding author: a.c.loyolacaetanorios@tudelft.nl



1 development phase provides criteria and guidelines for planning operational strategies, and  
2 establishes a hierarchy based on their optimization potential.

3 **Keywords:** UHS, depleted gas fields, operational strategies, development planning, site screening,  
4 Bunter sandstone

## 5 1 Introduction

6 Underground hydrogen storage (UHS) is an alternative for large-scale hydrogen storage, enabling  
7 seasonal balancing of supply and demand for applications such as energy systems and industrial  
8 feedstock. Numerical models of UHS [e.g. 38, 41] and recent pilot projects [3, 10] indicate that  
9 hydrogen gas could be effectively stored in salt caverns, aquifers, or depleted gas fields to be later  
10 recovered in periods of high energy demand [43].

11 The North Sea hosts hundreds of depleted gas fields, several of which are planned to be decom-  
12 missioned and repurposed to support greenhouse gas reduction. Current initiatives in the region  
13 include emerging projects for the permanent capture and storage of CO<sub>2</sub> [e.g. 1, 2] and the expansion  
14 of offshore wind energy capacity [9, 7]. The geological storage of hydrogen is also being assessed as  
15 an alternative to enhance energy security and provide seasonal flexibility for the expanding wind  
16 farms [22, 17].

17 The successful performance of a UHS operation depends on the effective containment of hydro-  
18 gen within geological traps and on the recovery of the stored gas with minimal loss. Moreover, the  
19 produced gas must have a level of purity that meets the requirements of its intended applications [6].  
20 In part, meeting these performance requirements depends on the selection of an appropriate geolog-  
21 ical formation, which must ensure sufficient storage capacity and deliverability [39, 50], and provide  
22 an environment that is not prone to hydrogen loss through mechanisms such as (bio)geochemical  
23 reactions, capillary trapping, and gravity override [19].

24 To support the procedure for site screening and selection, we have recently investigated the  
25 geological controls on the performance of UHS in depleted gas fields [29]. We targeted, as a case  
26 study, the Bunter Sandstone, a formation that hosts tens of depleted gas fields in the North Sea.  
27 We performed several numerical simulations of UHS in the ensemble of geological models designed  
28 by Alshakri et al. [4], which were extended to account for reservoir thickness, depth and dip. This  
29 model ensemble presents 32 plausible realizations (geological scenarios) for key geological features  
30 of the Bunter, considering their uncertainty. For this ensemble, the main geological controls on UHS  
31 performance were the thickness of the reservoir and of the sedimentological layers, and reservoir dip,  
32 which control the strength of buoyancy forces. The lateral continuity of low-permeability mudstones  
33 and of aeolian sandstones were also key controlling factors, because the former can act as baffles that  
34 compartmentalize flow and the latter promote easier spreading of the hydrogen at the top of the  
35 reservoir. All of these controlling geological features can either boost or mitigate gravity override,  
36 the main source of hydrogen loss observed in these models. Based on these insights, we proposed,  
37 as a site-screening criterion, a modified gravity number that incorporates geological heterogeneities.

38 These conclusions were drawn for a specific set of operational conditions, including a fully per-  
39 forated well, a given depletion level, and operation at full storage and recovery capacity. However,  
40 the performance of an UHS operation is not dictated by geology alone, but also by the development  
41 strategy itself. The effect of operational parameters on UHS performance in aquifers and depleted  
42 oil and gas fields has been subject to several studies. The most commonly tested strategies include  
1 well placement and perforation [41, 30, 35, 17]; the duration and target rates of cyclic operations



[35, 23, 49, 13, 5]; the amount and composition of the cushion gas [30, 23, 49, 13]; and the depletion level [23, 49].

However, these studies evaluate operational strategies in a single reservoir, whether synthetic or real, which makes their conclusions case-specific. Consequently, they do not provide generalizable engineering guidelines to optimize UHS while accounting for geological uncertainty that is captured by considering different geological scenarios. This generalization remains difficult when considering all studies collectively, partly because they often report divergent effects for certain operational parameters, such as the best cushion gas composition or the impact of higher flow rates [23, 49]. These discrepancies exist because each study considers different residual fluids, operations and geology.

On the other hand, there is agreement regarding the impact of some strategies on the performance of UHS. For example, there are multiple reports on the improvement of UHS performance when the well is placed updip [41, 35] and with shorter idle periods [23, 49]. Different studies also report higher purity when using hydrogen as cushion gas [30, 49]. Still, even these cases require a more systematic analysis to translate these findings into practical engineering guidelines. Such an analysis would benefit from identifying which strategies have the greatest potential impact on performance and should therefore be prioritized in development planning.

Furthermore, reservoir-specific findings provide a limited understanding of the interactions between geology and operational strategy. For optimization of development, it is useful to determine which operational choices are best suited to a specific geological scenario and geological heterogeneity. For site screening, it is valuable to understand if optimal operational choices can compensate for geological scenarios that are more susceptible to hydrogen losses; or, conversely, if poor operational decisions can undermine the potential of a geological formation with good reservoir properties that should lead to high performance.

This work aims to address these gaps. To do so, we use numerical models of flow and transport to simulate different UHS operational strategies for the ensemble of geological models of the Bunter sandstone designed by Alshakri et al. [4] and extended by [29]. We consider eight distinct operational tests, each modifying an operational strategy that we adopted previously [29]. These operational strategies include the depletion level, the amount of stored hydrogen, the amount and composition of the cushion gas, the duration of the idle period, the target injection and withdrawal rates, the length of the well perforation, and a two-well strategy for reinjecting the co-produced methane. To the best of our knowledge, this combination of parameters is investigated here for the first time

Using this approach, this study pursues the following objectives, each providing a novel contribution to the topic of development planning and site screening for UHS in depleted gas fields: (i) evaluate the impact on UHS performance of different operational strategies in varying geological scenarios; (ii) assess the sensitivity of these impacts to geology; (iii) update our earlier screening criteria [29] to account for operational strategies; and (iv) provide general guidelines for the development of UHS that integrate geological aspects. These guidelines will provide criteria for development planning and establish a hierarchy of operational strategies based on their potential influence on performance.

This paper is structured as follows. Section 2 presents the computational models, including the geological model ensemble and the numerical model. Section 3 recapitulates the main results and findings of the tests performed by Loyola et al. [29] to assess the geological controls on UHS, here referred to as the reference simulations. Section 4 presents and discusses the results of the operational tests. Section 5 uses these results to propose updated screening criteria and a framework for development planning of UHS in depleted gas fields. Finally, Section 6 presents the conclusions



2 and perspectives for future work.

## 3 2 Computational models

4 To analyze the impact of UHS operational strategies on different geological scenarios of the Bunter  
5 sandstone, we employ the open-access geological models developed by Alshakri et al. [4] and later  
6 modified by Loyola et al. [29]. These models are used to simulate UHS operations with the Open  
7 Delft Advanced Terra Simulator (open-DARTS) [48].

8 Section 2.1 presents the ensemble of geological models, and Section 2.2 describes the open-  
9 DARTS numerical model.

### 10 2.1 Geological models

11 The Bunter Sandstone is a fluvial–aeolian formation of Triassic age that extends across several  
12 regions of Europe, notably the North Sea, where it hosts several gas fields. Alshakri et al. [4]  
13 identified six main stratigraphic bodies within the Bunter: multistorey, multilateral, and cemented  
14 fluvial sandstones; aeolian sandstones; channelized fluvial sandstones; floodplain and sabkha (silty)  
15 mudstones; and clay-rich lacustrine mudstones (Figure 1).

16 These sedimentological bodies vary considerably in their volumetric proportions, thicknesses  
17 and petrophysical properties, as interpreted from seismic, well logs and core-sample data [e.g.  
18 33, 45, 46, 12]. Based on an extensive review of such data, Alshakri et al. [4] used the Rapid Reservoir  
19 Modeling (RRM) software [37, 21] to design the ensemble of 32 geological models that we use in  
20 our simulations. This ensemble was built using a factorial Design of Experiment (DOE) approach,  
21 in which selected factors are varied between low and high settings to quantify their impact on a  
22 given response. Eight key heterogeneities of the Bunter were included, mostly associated with the  
23 thickness, lateral continuity, and permeability of its main stratigraphic bodies. Each combination  
24 of these factors results in a unique geological scenario.

25 In addition to these sedimentological properties, the Bunter also presents significant spatial  
26 variation in burial depths and formation thickness [12]. Loyola et al. [29] extended the DOE of  
27 Alshakri et al. [4] to include other factors such as reservoir thickness and structural dip, establishing  
28 low and high values for these values based on the well data of Dutch Triassic formations compiled by  
29 Korevaar et al. [26]. Table 1 lists all the factors varied in the ensemble, while Table A1 in Appendix  
30 A presents the extended DOE. The rationale for the low and high settings of these factors is detailed  
31 in Alshakri et al. [4] and in the Supplementary Material of Loyola et al. [29].

32 The resulting models have dimensions of 600 m  $\times$  600 m in the x–y directions and a thickness  
33 of 59 m or 176 m in the z-direction, depending on it assuming a high or low setting in the DOE.  
34 These lateral dimensions of 600 m  $\times$  600 m are compatible with the dimensions of small gas fields  
35 in the North Sea that are considered for UHS.

36 Figure 1 shows Models 5 and 12 as two representative examples from the model ensemble. The  
37 reservoir depth is fixed at 1500 m in all cases. We have previously simulated the model ensemble  
38 considering reservoir depths of 1500 m and 3000, and concluded that higher depths slightly decrease  
39 UHS performance metrics due to lower gas compressibility and higher density contrasts between  
40 H<sub>2</sub> and CH<sub>4</sub>. For further details on this comparison, the reader is referred to [29].



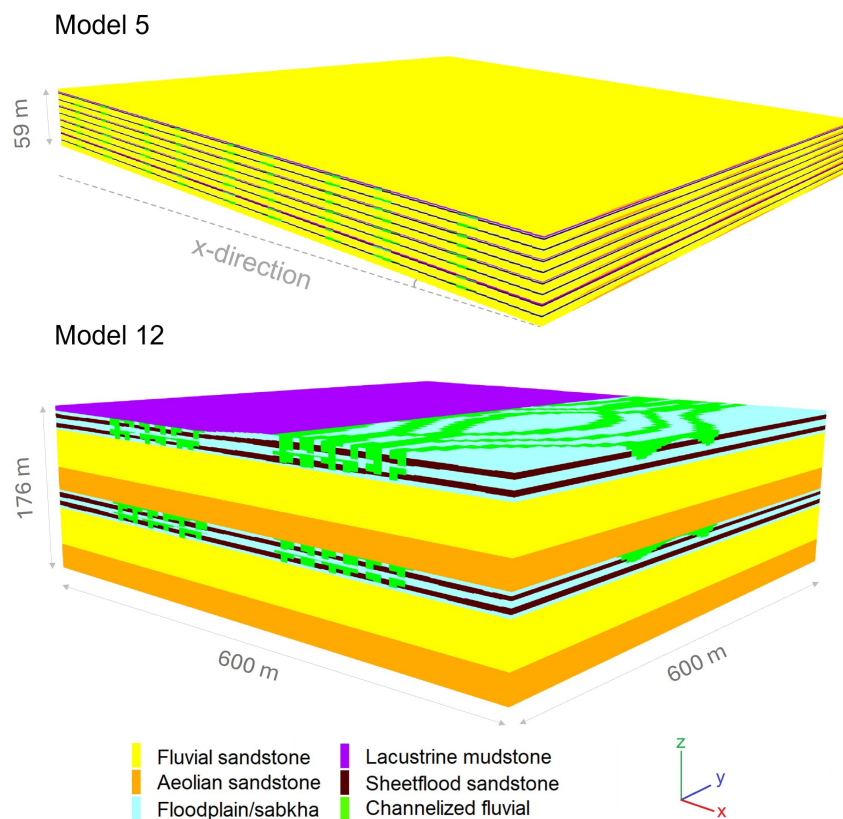


Figure 1: Models 5 and 12 of the geological model ensemble designed by Alshakri et al. [4] and modified by Loyola et al. [29]. Model 5 has low layer and reservoir thickness and a high dip, whereas Model 12 has high layer and reservoir thickness and no dip. See Table 1 for the full description of the geological factors and Table A1 for their settings.

## 2.2 Numerical model

This section describes the numerical model implemented in the open-DARTS framework and the set of simulations performed. Section 2.2.1 presents the main assumptions and the mathematical formulation of the model, and Sections 2.2.2 to 2.2.4 describe the setup of the model, including the initial conditions, fluid and rock properties, mesh, boundary conditions, and the well model.

The ensemble of geological models is used to perform several operational tests, each corresponding to a set of simulations that assess the impact of a different operational strategy on the UHS performance metrics for the model ensemble. These operational tests are compared to a set of simulations referred to as the reference simulations, which correspond to the simulations performed by Loyola et al. [29]. Section 2.2.5 presents the operational parameters used in the reference simulations, Section 2.2.6 describes the operational tests, and Section 2.2.7 introduces the performance



Table 1: Factors analyzed in the Design of Experiments (DOE) and their low and high settings. Factors A to F were used by Alshakri et al. [4] to build the ensemble of 32 geological models. The remaining factors were added by Loyola et al. [29] to extend their DOE. In Factor G,  $k_v$  and  $k_h$  denote the vertical and horizontal permeability, respectively. Modified from Loyola et al. [29].

Factor Id	Factor	Low *	High *
A	Thickness of layers	Fluvial	3.4/10 m
		Floodplain/ Sabkha	1.7/5 m
		Aeolian	1.7/5 m
		Lacustrine	0.7/2 m
B	Lateral continuity of aeolian bodies	Discontinuous lens	Continuous sheet
C	Lateral continuity of lacustrine layers	Discontinuous sheet	Continuous sheet
D	Proportion of channelized fluvial sandbodies in floodplain/sabkha	17 %	33 %
E	Lateral connectivity of channelized fluvial sandbodies in floodplain/sabkha	Isolated clusters	Connected network
F	Lateral continuity of sheetflood sandbodies in floodplain/sabkha	Discontinuous lens	Continuous sheet
G	$k_v/k_h$ ratio of fluvial sandbodies	0.05	0.5
H	Permeability of lacustrine layers	0.001 mD	0.01 mD
I	Reservoir thickness	59 m	176 m
J	Reservoir dip	0°	3°

\* The two values separated by bars correspond to the thickness of layers when the reservoir thickness is low and thigh, respectively.

2 metrics used for comparison.

### 3 2.2.1 Mathematical description

4 The reservoirs are assumed to be depleted methane ( $\text{CH}_4$ ) gas reservoirs with no aquifer connection.  
 5 We solve the problem of injection and production of hydrogen ( $\text{H}_2$ ) in these reservoirs with a one-  
 6 phase (gas), two-component isothermal flow and transport model. The mass conservation equation  
 7 is described as

$$\frac{\partial(\phi x_c \rho_p)}{\partial t} + \nabla \cdot (x_c \rho_g \mathbf{u}_g + \phi \rho_p \mathbf{J}_c) - q_c = 0. \quad (1)$$

8 Here, the subscript  $c$  denotes a component ( $\text{H}_2$  and  $\text{CH}_4$ ), the subscript  $g$  refers to the gas phase,  $\phi$   
 9 is the effective rock porosity,  $x_c$  is the molar concentration of component  $c$ ,  $\rho_g$  is the molar density  
 1 of the gas phase,  $\mathbf{u}_g$  is the velocity of the gas phase,  $\mathbf{J}_c$  is diffusive flux of component  $c$  and  $q_c$



2 denotes source of the component  $c$ .

3 The phase velocity  $\mathbf{u}_g$  is given by Darcy's law as

$$\mathbf{u}_g = -\frac{\mathbf{K}}{\mu_g}(\nabla p_g - \rho_g \mathbf{g}), \quad (2)$$

4 where  $\mathbf{K}$  is the permeability tensor,  $\mu_g$  the viscosity of the gas phase and  $\mathbf{g}$  is the gravity vector.

5 The diffusive flux  $\mathbf{J}_c$  is given by Fick's law as

$$\mathbf{J}_c = -D_c \nabla x_c, \quad (3)$$

6 where  $D_c$  is the molecular diffusion coefficient of component  $c$ .

7 The open-DARTS model employs a cell-centered Finite Volume Two Point Flux approxima-  
8 tion scheme for the spatial discretization of both fluxes and a fully implicit scheme for the time  
9 discretization [31]. All simulations were performed on the DelftBlue supercomputer [8].

10 Note that depleted gas fields with no significant aquifer contribution are still expected to contain  
11 a residual amount of water. Although this water is immobile, it can give rise to capillary and  
12 solubility trapping of  $\text{H}_2$  and influence its mobility through interfacial phenomena. These effects  
13 are neglected in our single-phase flow formulation.

### 14 2.2.2 Initial reservoir conditions

15 The reservoir temperature is set to 55 °C, computed for the depth of 1500 m using the temperature-  
16 depth relationship derived for the borehole data from the Netherlands Oil and Gas Portal (NLOG)  
17 [34] (see the Supplementary Material of [29]). For a depth of 1500 m, we estimate a hydrostatic  
18 pressure of 150 bar and assume it to be the original reservoir pressure before depletion. This  
19 hydrostatic pressure is used to define an initial pressure at the start of the UHS operation, based  
20 on a specified depletion level, to be defined in Sections 3 and 4.

### 21 2.2.3 Rock and fluid properties

22 Table 2 presents the porosity and the intrinsic permeability of the sedimentological layers as defined  
23 by Alshakri et al. [4] and Loyola et al. [29]. The permeability is considered to be isotropic for all  
24 sedimentological layers except the fluvial sandstones. For these latter, Table 2 gives the horizontal  
25 permeability, and the vertical permeability is computed according to the given permeability ratio,  
26 which is a factor in the DOE (Table 1). The permeability values in Table 2 are consistent with  
27 the lower-end of the permeability ranges reported by Foote et al. [14, Figure 9] for the considered  
28 sedimentological layers.

29 The gas density is computed using the Peng-Robinson equation of state. The gas viscosity  
30 is estimated using the datasets from Hassanpouryouzband et al. [18] and the NIST Chemistry  
31 WebBook [28], which provide viscosity values for various combinations of pressure, temperature,  
32 and gas composition. We use the multilinear interpolation scheme implemented in open-DARTS  
33 [24, 32] to interpolate viscosity at arbitrary states. For further details, see Figure S3 in [29].

34 The molecular diffusion coefficient is assumed constant and equal to 0.078 m<sup>2</sup>/day, as obtained  
1 from the correlation proposed by Kobeissi et al. [25]. The pressure input for this correlation  
2 corresponds to the average of the minimum and maximum borehole pressures (Table 3).



Table 2: Intrinsic permeability and porosity of the sedimentological bodies present in the Bunter sandstone models.

Geobody	Porosity (%)	Permeability (mD)
Lacustrine mudstone	5	0.001 or 0.01 *
Floodplain and sabkha mudstone	7	1
Sheetflood fluvial sandstone	7	1
Fluvial sandstone**	17	500
Aeolian sandstone	24	3000

\* Lacustrine mudstone permeability is a factor in the DOE

\*\* Permeability in horizontal directions

### 2.2.4 Mesh, boundary conditions, and wells

The finite volume grid is fully structured, containing  $71 \times 71 \times 132$  cells for models with low reservoir thickness and  $71 \times 71 \times 396$  cells for those with high reservoir thickness. The grid cell size is the same across all models of the ensemble. This resolution was defined by Loyola et al. [29] based on mesh convergence studies. In models with high dip, the dip is implemented by translating grid columns in a stepwise manner along the x-direction, so that the highest elevation is reached at the minimum x-coordinate (Figure 2 in [29]).

All reservoir boundaries are closed (no-flow). These boundary conditions imply negligible leakage of  $H_2$  through the caprock and other sealing layers. The validity of this assumption should be assessed for target reservoirs based on an evaluation of the sealing properties of the cap rock and overburden, including the role of potential faults.

UHS operations are simulated in a single vertical well with a diameter of 0.16 m. The well is positioned at the coordinates (13 m, 300 m) in the x-y plane, so that it perforates cells located at center of the y-axis and close to the minimum x-coordinate. In models with high dip, this positioning ensures that the well is located structurally updip.

$H_2$  injection and production are modeled by defining target flow rates at the well (source terms). The flow transfer between the well and the reservoir is modeled following the formulation by Peaceman [36], with no skin factor considered. When the bottom-hole pressure (BHP) reaches its upper or lower limit, the flow rate is adjusted to ensure that the respective pressure constraints are not violated.

### 2.2.5 Operational parameters in the reference simulations

The UHS operations of the reference simulations consist of two phases. The first phase is an initialization period during which pure  $H_2$  is injected as cushion gas. This period ends when the minimum BHP is reached in the well. Following the initialization, the cyclic storage operation starts. In the reference simulations, each cycle lasts one year and comprises a six-months injection period followed by three-months idle and production periods. The idle periods correspond to a shut-in period where zero flow rates are assigned to the well. The minimum and maximum BHPs are 75 bar and 150 bar, respectively.

Table 3 summarizes the operational parameters in the reference simulations, including well perforation, initial reservoir pressure, BHP limits, and target rates. The well is fully perforated



throughout the thickness of the reservoir, and the depletion level is set to two-thirds of the hydrostatic pressure, resulting in an initial pressure of 50 bar.

The target rates in Table 3 were defined to ensure that the reservoirs operate at their full storage and recovery capacities, constrained by the minimum and maximum BHP. The target rates for the models with high reservoir thickness were three times those for the models with low reservoir thickness. This scaling ensures that all models operate at comparable flow rates, H<sub>2</sub> pore volume occupation, and pressure ranges, allowing for a reliable comparison across the different geological scenarios [29].

Table 3: Operational parameters used for the reference simulations. The target rates and well perforation differ between the low- and high-reservoir-thickness models. The well perforation corresponds to the reservoir thickness in each case, and the target rates are scaled accordingly.

Initial pressure (bar)	50	
Minimum/maximum BHP (bar)	75/150	
	Low res. thick.	High res. thick.
Target rate - Initialization (Mmol/day)	35	105
Target rate - Injection (Mmol/day)	52	156
Target rate - Production (Mmol/day)	104	312
Well perforation (m)	59	176

### 2.2.6 Operational tests

Table 4 presents the eight operational tests performed in this study. These tests modify the operational parameters of the reference simulations. If any change in an operational parameter is not explicitly stated, that parameter remains identical to the reference simulations.

Test 1 (Depletion level) assesses the impact of increasing the depletion level of the reservoirs to 90 % of their original hydrostatic pressure. This results in an initial reservoir pressure (at the start of the operation) of 15 bar. The minimum BHP is reduced to 40 bar. Since, in the initialization phase, the H<sub>2</sub> cushion gas is injected until the minimum bottomhole pressure is reached, this ensures additional pressure support of approximately 25 bar provided by the cushion gas, similarly to the reference simulations. This change in the minimum BHP is based on the assumption that lower working pressures do not compromise reservoir containment or the deliverability of the well system, since such pressures were already achieved during CH<sub>4</sub> production.

Test 2 (Injected amount) assesses the impact of reducing the amount of H<sub>2</sub> injected during the cyclic operation, i.e. the working volume of H<sub>2</sub>. In the reference simulations, the reservoirs operate at full storage and recovery capacity, i.e. the well pressure varies between the minimum and maximum BHPs during the cyclic operation. However, UHS may involve reservoirs whose storage capacity exceeds the projected storage demand. To investigate an operation below storage capacity, Test 2 reduces the target mass of H<sub>2</sub> injected during the cyclic operation by half. The target mass rates are kept unchanged, while the duration of the injection and production periods are reduced by half. The amount of injected H<sub>2</sub> during the initialization phase remains unchanged.

Test 3 (No H<sub>2</sub> cushion gas) omits the initialization phase, starting the storage operation directly with the injection–production cycles. We assume that the decision to not use cushion gas implies



Table 4: The performed operational tests.

Test Id	Test Name (%)	Description
1	Depletion level	Initial reservoir pressure is set to 10 % of the hydrostatic pressure. Initial pressure = 15 bar, minimum BHP = 40 bar.
2	Injected amount	Cyclic injection of H <sub>2</sub> is reduced by 50%. Same target rates, injection and production duration are decreased by 50%
3	No cushion gas	No initialization phase. Minimum BHP = 50 bar.
4	Cushion gas composition	The cushion gas is a mixture of 50% CH <sub>4</sub> and 50 % H <sub>2</sub> .
5	Well perforation	Well perforation is half of the reservoir thickness.
6	Reinjection of CH <sub>4</sub>	Co-produced CH <sub>4</sub> is reinjected in the reservoir.
7	No idle period	No idle period in the cyclic operation.
8	Target rate	Cycle flow rates increased by a factor of 2. Injection and production periods are decreased by 50%.

22 that no pressure support is required to ensure well deliverability or safe containment. Consequently,  
23 the minimum bottomhole pressure is set equal to the initial reservoir pressure of 50 bar.

24 Test 4 changes the composition of the cushion gas injected during initialization, using a mixture  
25 of 50% H<sub>2</sub> and 50 % CH<sub>4</sub>, in terms of molar fraction.

26 Test 5 (Well perforation) reduces the length of the perforated interval to half of the reservoir  
27 thickness. This reduced perforation is connected to all sedimentological layers present on the top  
28 half of the reservoir (see the H<sub>2</sub> well in Figure 2).

29 Test 6 (Reinjection of CH<sub>4</sub>) implements a strategy for reinjecting the co-produced CH<sub>4</sub>. This  
30 reinjection may be required due to the lack of an alternative to handle the co-produced gas, for  
31 environmental compliance, or for increasing reservoir pressure. To promote the separation of H<sub>2</sub>  
32 and CH<sub>4</sub>, the well configuration shown in Figure 2 is used. The H<sub>2</sub> well remains at the same x-y  
33 coordinates and is perforated over half of the reservoir thickness, as in Test 5 (Well perforation). A  
34 second well (CH<sub>4</sub> well) is placed on the opposite side of the reservoir and perforated until its highest  
35 depth. This second well is used for reinjecting the CH<sub>4</sub> produced from the H<sub>2</sub> well. The length of  
36 the perforation of the CH<sub>4</sub> well is equal to  $\frac{1}{6}$  of the reservoir thickness. This length was defined to  
37 avoid pressure interference with the H<sub>2</sub> well. During the production period, CH<sub>4</sub> co-produced at  
38 the H<sub>2</sub> well is accumulated for 10 days and reinjected in the CH<sub>4</sub> well over periods of 1 to 2 days,  
39 depending on the amount of CH<sub>4</sub> and the target rates. The period of 10 days was set to ensure  
40 that the target rates for reinjection of CH<sub>4</sub> are high-enough to avoid numerical convergence issues  
41 in the simulation.

42 Test 7 (No idle period) does not have an idle period. While the reference simulations have a  
43 three-months idle period between the injection and recovery phases, the cyclic operation in Test 7  
44 alternates between a six-months injection and three-months production.

45 Test 8 (Target rates) doubles the target rates of the injection and production periods, while  
46 reducing their durations by half so that the total amount of injected H<sub>2</sub> remains equal to that of  
1 the reference case.



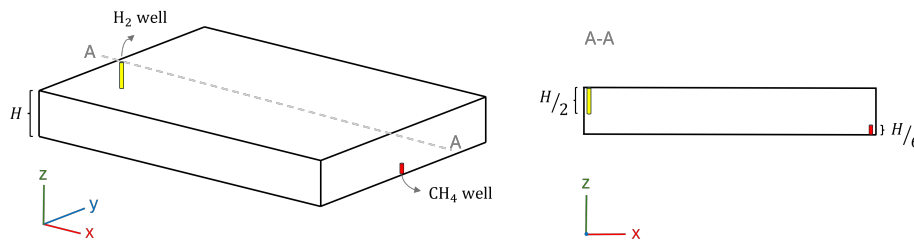


Figure 2: Configuration of the wells in Test 6 (Reinjection of CH<sub>4</sub>).

Although the target rates and the duration of the idle period are tested here as operational strategies, they are not design parameters per se, as they cannot be flexibly planned in UHS operations. Rather, they are determined by the schedules of H<sub>2</sub> production and demand arising from the use case that justifies the need for a H<sub>2</sub> storage solution. Thus, they are tested here to assess whether external variables that determine H<sub>2</sub> production and demand may affect the performance of UHS operations.

### 2.2.7 Performance metrics

Four performance metrics are computed in the simulations to quantify the efficiency of an operational strategy: cycle recovery factor (*RF*), ultimate recovery factor (ultimate *RF*), cycle mass purity (*MP*) and flow purity (*FP*). The Recovery Factor (*RF*) of cycle *i* is given by

$$RF^i = \frac{M_{prodH_2}^i}{M_{injH_2}^i}, \quad (4)$$

where  $M_{prodH_2}^i$  and  $M_{injH_2}^i$  are the produced and injected mass of hydrogen, respectively, in cycle *i*, respectively. The ultimate *RF* is computed as

$$RF = \frac{\sum_i M_{prodH_2}^i}{\sum_i M_{injH_2}^i}, \quad (5)$$

Mass purity (*MP*) of cycle *i* is given by

$$MP^i = \frac{M_{prodH_2}^i}{M_{rec}^i}, \quad (6)$$

where  $M_{prodH_2}^i$  and  $M_{rec}^i$  are the produced mass of H<sub>2</sub> and total produced mass of fluids in cycle *i*, respectively. The flow purity *FP* at time *t* of the withdrawal phase of cycle *i* is given by

$$FP^i(t) = \frac{Q_{H_2}^i(t)}{Q_t^i(t)}, \quad (7)$$

where  $Q_{H_2}^i$  and  $Q_t^i$  are outflow rates of hydrogen and total outflow rates in time *t* of the production phase of cycle *i*, respectively.

Throughout this text, when we refer to UHS performance we refer specifically to these metrics that measure H<sub>2</sub> recovery and purity.



### 3 Summary of the reference simulations

We present here a summary of the results of the reference simulations [29] that are most relevant to the present study, as well as their interpretation.

The reference simulations resulted in a wide range of performance metrics for the model ensemble. The variability of these metrics is highest in cycle 1 and decreases as the operation progresses (Figure 3). This variability is due to the geological heterogeneities captured by the ensemble. As the injection-production cycles increase, these heterogeneities become less influential because  $\text{CH}_4$  initially in place is progressively replaced by  $\text{H}_2$  and there is sufficient time for  $\text{H}_2$  to enter the lower-permeability layers.

We frequently refer to the performance in cycle 1 because this is the most critical stage of the operation — where the performance metrics of each model are at their minimum, and their variability is highest. From here on, we denote the recovery factor and methane purity of cycle 1 as  $RF_1$  and  $MP_1$ , respectively.

In the reference simulations,  $RF_1$  range from 70 % to 96 %,  $MP_1$  from 71 % to 96 %, and the ultimate  $RF$  from 89 % to 96 %. Models 5 and 12 (Figure 1) exhibited the highest and lowest values for these metrics, respectively. These two models are representative of the geological factors that control UHS performance. Loyola et al. [29] identified the thickness of the sedimentological layers, reservoir thickness, and dip as the three most influential factors affecting the performance metrics for cycle 1. Model 5 has low layer thickness, low reservoir thickness, and high dip, whereas Model 12 has high layer and reservoir thickness and no dip.

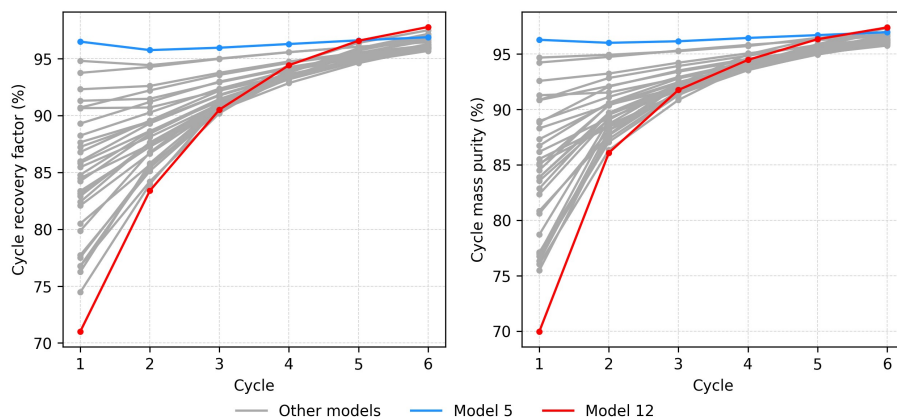


Figure 3: Cycle recovery factor and mass purity observed in the reference tests. Models 5 and 12 (Figure 1) are highlighted with distinct colors, as they presented the highest and lowest performance metrics in cycle 1, respectively. Results for the other models are shown in grey to represent the ensemble as a whole.

The geological controls identified by Loyola et al. [29] influence UHS performance through their effect on gravity-driven mechanisms. The displacement of  $\text{CH}_4$  by  $\text{H}_2$  naturally carries a risk of unstable displacement due to the significantly lower viscosity and density of  $\text{H}_2$ . Here, the terms unstable displacement or unstable fronts refer specifically to gravity override, in which  $\text{H}_2$ , driven by buoyancy forces, migrates upward and spreads laterally along the reservoir top. This instability



4 is directly related to  $H_2$  loss and  $CH_4$  production, since the  $CH_4$  that is not efficiently displaced can  
5 reach the well and be produced.

6 The degree of instability, however, is strongly controlled by the geological scenario. This is  
7 illustrated by comparing Figures 4 and 5, which show cross-sectional views of the  $H_2$  plume at  
8 different stages during cycle 1 for Models 5 and 12, respectively.

9 In Model 5, the  $H_2$  plume develops a relatively stable front with the resident  $CH_4$ , approaching a  
10 piston-like displacement during the initialization phase. During the cyclic operation, some gravity  
11 override occurs away from the well, but viscous forces driving longitudinal migration outweigh  
12 buoyancy forces through most of the reservoir. The buoyancy forces are weak in this model because  
13 the sedimentological layers are thin. In addition, the continuous lacustrine mudstones in Model 5  
1 further mitigate buoyancy forces by compartmentalizing flow, and the high dip helps to keep  $CH_4$   
2 segregated toward the bottom of the reservoir.

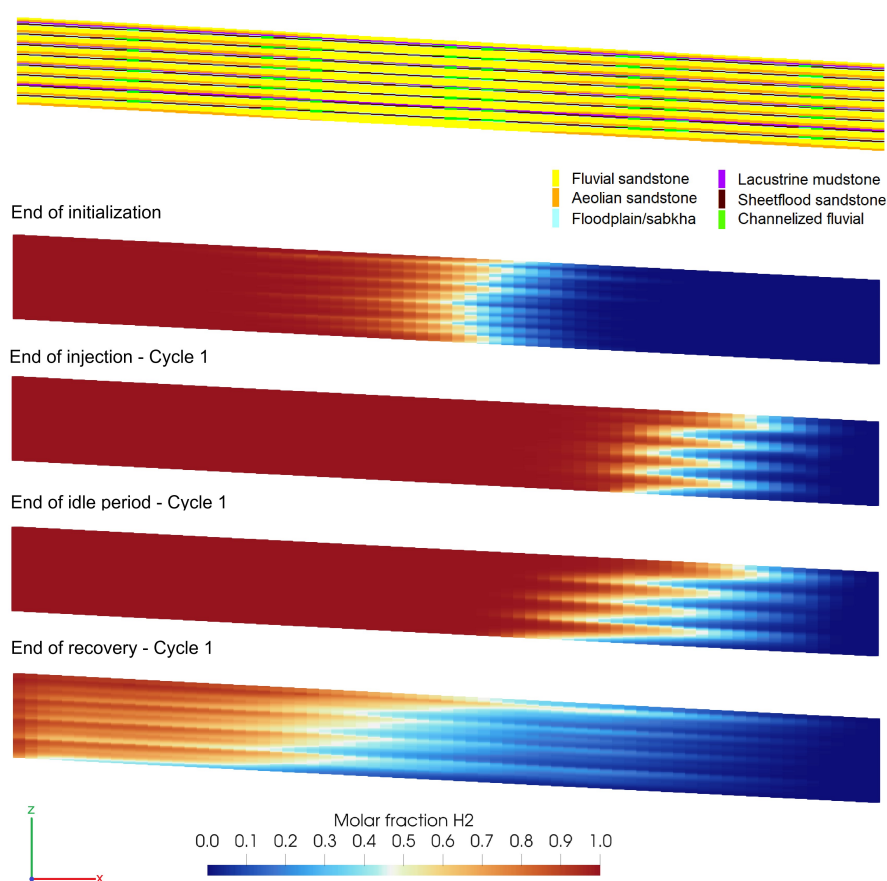


Figure 4: Cross-sectional view of the sedimentological layers and the  $H_2$  plume in the reference simulation of Model 5 during different stages of cycle 1.

3 In contrast, Model 12 exhibits pronounced gravity override already during the initialization



4 phase, and this instability develops much closer to the well. This behavior results from stronger  
5 buoyancy forces, which are proportional to the thickness of the depositional cycles (i.e., the repeating  
6 pattern of sandstone and mudstone couplets). The occurrence of gravity override is also favored by  
7 the zero dip in this model. As  $H_2$  spreads along the reservoir top,  $CH_4$  rapidly approaches the well  
8 and is produced, leading to the low performance metrics observed in this model.

9 In the absence of significant viscous forces, the interface between fluids of contrasting density  
10 tends toward a hydrostatic equilibrium configuration, leading to a horizontally segregated front.  
11 Model 12 approaches this limiting condition by the end of the idle period, rendering the well, which  
12 is perforated across the entire reservoir thickness, particularly exposed to  $CH_4$  during production.

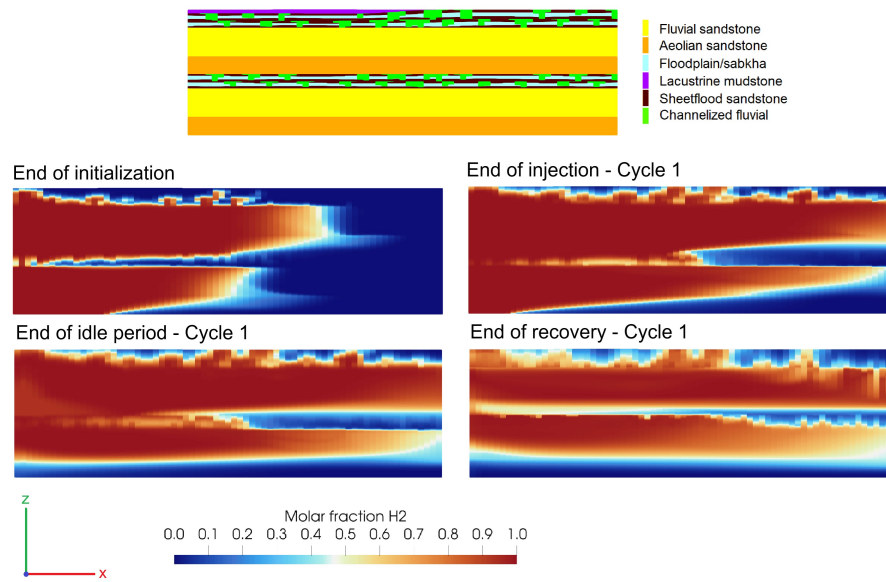


Figure 5: Cross-sectional view of the sedimentological layers and the  $H_2$  plume in the reference simulation of Model 12 during different stages of cycle 1.

### 13 3.0.1 Modified gravity number

14 Based on the gravity-controlled behavior of the reference tests, Loyola et al. [29] adapted the gravity  
15 number derived by Shook et al. [42] to consider the key geological heterogeneities of the Bunter  
16 sandstone for UHS. This modified gravity number is given by

$$N_g = \frac{k_x \lambda \Delta \rho g \cos \alpha H}{u L}, \quad (8)$$

17 where  $k_x$  is the upscaled horizontal permeability of the reservoir (here computed with flow  
1 based upscaling in RRM),  $\lambda$  is the mobility of the injected phase,  $\Delta \rho$  is the density difference  
2 between the two fluids,  $g$  is the gravitational acceleration,  $\alpha$  is the dip angle,  $u$  is the velocity of  
3 the injected fluid,  $H$  is the thickness of the depositional cycle bounded by mudstone layers, and  $L$   
4 is the length of the reservoir. The modifications proposed by Loyola et al. [29] include the use of



5 the upscaled permeability and the replacement of the thickness of the reservoir with the thickness  
6 of the depositional cycles.

7 The modified  $N_g$  correlates strongly with the performance metrics computed for the Bunter  
8 sandstone model ensemble, especially when clustering the reservoirs according to their dip [29].  
9 In addition to the results presented by Loyola et al. [29] for  $RF_1$ , we present here the correlation  
10 between  $N_g$  and the ultimate  $RF$  of the reference test, measured by the Spearman coefficient.

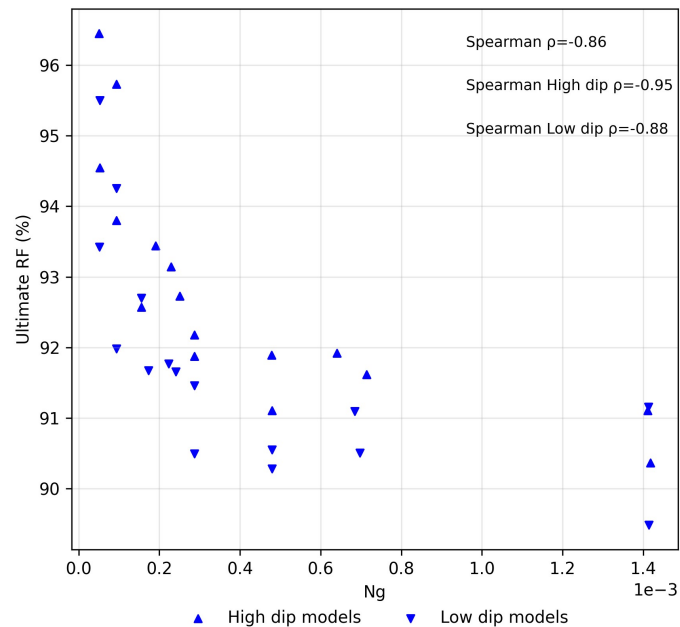


Figure 6: Spearman correlation between the ultimate Recovery Factor ( $RF$ ) of the reference tests and the modified gravity number ( $N_g$ ) proposed by Loyola et al. [29]. The Spearman coefficient is presented for all the models, low-dip models and high-dip models.

## 11 4 Results of the operational tests

12 Figure 7 shows the range of  $RF_1$ ,  $MP_1$ , and ultimate  $RF$  for the reference models and the opera-  
13 tional tests. Further detail on the evolution of performance in the operational tests can be found  
14 in Figures S1 to S7 of the Supplementary Material. Figure S8 presents the evolution of average  
15 reservoir pressures during the UHS operations for the operational tests.

16 To evaluate whether the modified  $N_g$  remains correlated to the performance metrics in each  
17 operational test, Table 5 shows the Spearman coefficients for the ultimate  $RF$  and  $N_g$ . In the  
18 Supplementary Material, Figures S9 to S11 present the correlation of  $N_g$  with  $RF_1$ ,  $MP_1$  and the  
1 ultimate  $RF$ . Except for Test 5 (Well perforation) and Test 6 (Reinjection of  $CH_4$ ), the correlation  
2 between  $N_g$  and the performance metrics is negative and strong in all tests, with absolute values  
3 greater than 0.8. Therefore, in all tests except those two, higher performance metrics generally  
4 correspond to lower  $N_g$  values and vice versa.



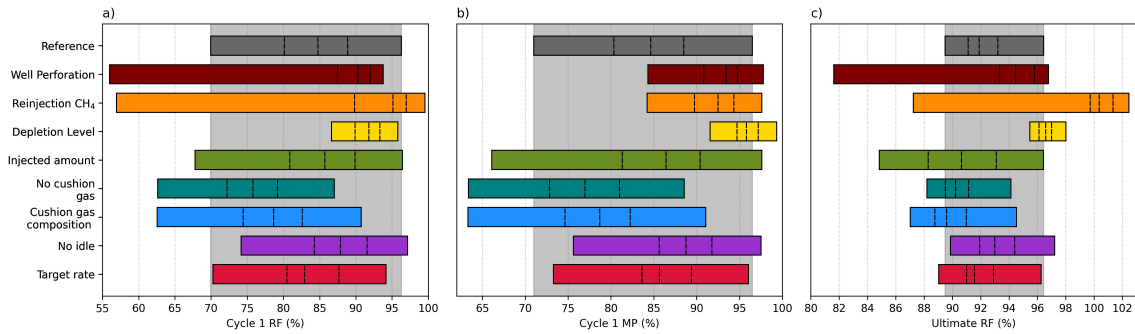


Figure 7: Range of variation of a) ultimate Recovery Factor ( $RF$ ), b)  $RF$  of cycle 1 and c) the mass purity ( $MP$ ) of cycle 1 in the reference simulations and operational tests. The left, middle, and right dashed lines crossing each bar correspond to the first, second and third quartiles of the data, respectively.

Table 5: Spearman coefficients between ultimate recovery factor and the modified gravity number for the reference and operational tests.

Test	Low dip	High dip
Reference	-0.88	-0.95
1 - Depletion Level	-0.84	-0.84
2 - Injected amount	-0.87	-0.88
3 - No cushion gas	-0.83	-0.93
4 - Cushion gas comp.	-0.95	-0.86
5 - Well perforation	0.40	0.41
6 - ReInjection of $CH_4$	-0.47	-0.12
7 - No idle	-0.96	-0.87
8 - Target rate	-0.95	-0.87

To analyze the impact of operational strategies under different geological conditions, the model ensemble is divided into two groups based on  $N_g$ . The lowest  $N_g$  group includes the eight models with the lowest  $N_g$  values (bottom quartile), while the highest  $N_g$  group includes the eight models with the highest  $N_g$  values (top quartile). Table 6 presents the average values for  $RF_1$ ,  $MP_1$  and ultimate  $RF$  for each group. It also presents the average value for  $G_g = k_x H \cos(\alpha)$ , which is the part of  $N_g$  that includes reservoir characteristics, namely the upscaled permeability  $k_x$ , the dip angle  $\alpha$  and the thickness of the depositional cycle  $H$ . Moreover, Figure 8 shows the average differences in the performance metrics between the operational tests and the reference cases, calculated for the highest  $N_g$ , lowest  $N_g$ , and the entire ensemble of 32 models. All highest  $N_g$  models have high thickness of the reservoir and of the sedimentological layers, while all lowest  $N_g$  models have low setting for both factors in the DOE.

The next sections analyze and discuss these results for each operational test, with focus on: (i) the variations in the range of performance metrics induced by different operational strategies; (ii) the main flow mechanisms driving these variations; (iii) the interaction between operational



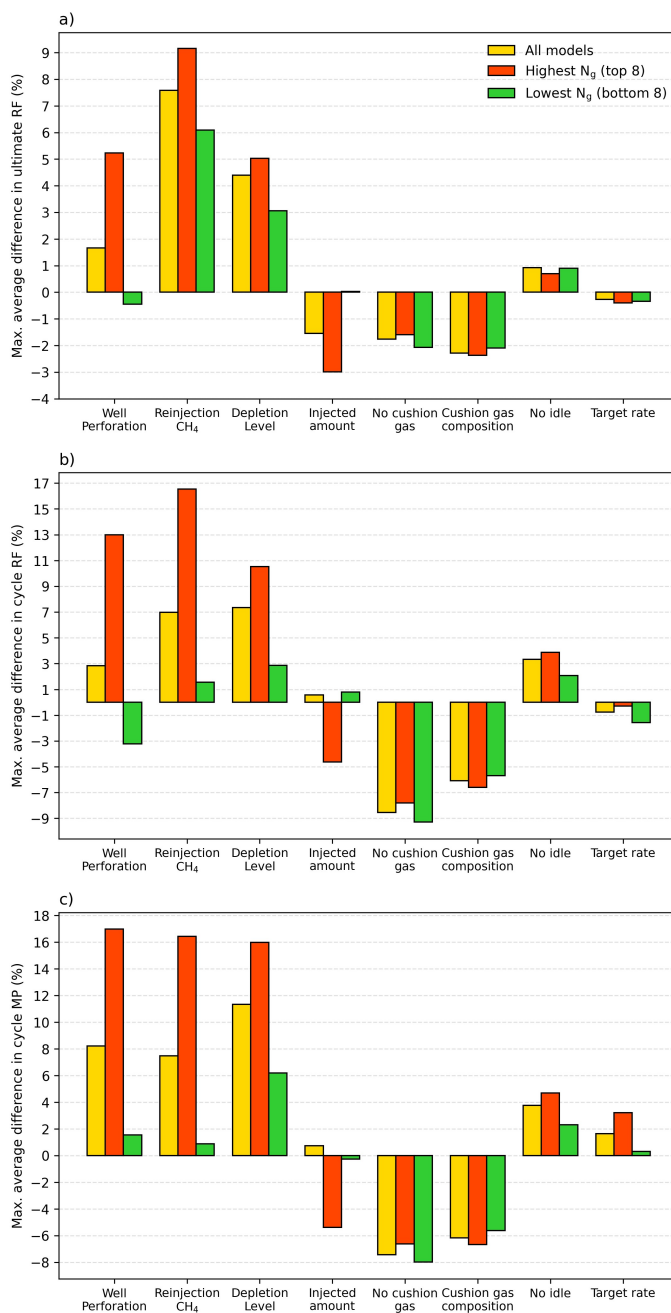


Figure 8: Average differences in the (a) ultimate recovery factor, (b) cycle recovery factor (*RF*) and (c) cycle mass purity (*MP*) between each operational test and the reference case as computed for the whole model ensemble, the lowest  $N_g$  models and the highest  $N_g$  models. The differences in cycle *RF* and cycle *MP* correspond to the cycle that presented the maximum average differences, which is cycle 2 for Test 2 (Injected amount of H<sub>2</sub>) test and cycle 1 for the other operational tests.

Open Access Article. Published on 25 June 2026. Downloaded on 6/26/2026 1:22:11 PM.  
This article is licensed under a Creative Commons Attribution 3.0 Unported Licence.



Environmental Science: Advances Accepted Manuscript

Table 6: Average geometrical component of the gravity number ( $G_g$ ), recovery factor of cycle 1 ( $RF_1$ ), mass purity of cycle 1 ( $MP_1$ ), and ultimate recovery factor (ultimate  $RF$ ) for the highest and lowest  $N_g$  groups, which include the eight models with the highest and lowest  $N_g$  values, respectively.

Group	Models	$G_g$ ( $m^3$ )	$RF_1$ (%)	$MP_1$	ultimate $RF$
Highest $N_g$	1,3,5,7,25,27,29,31	71312	78	78	90
Lowest $N_g$	10,12,14,16,18,20,22,24	4925	92	92	94

5 strategies and geology; and (iv) comparisons with findings from previous studies when pertinent.

#### 6 4.1 Test 1 — Depletion level

7 Compared to the reference simulation, the higher depletion level of 90% significantly improves the  
8 performance across the model ensemble. This improvement is most evident in the minimum values  
9 of the performance metrics (Figure 7), which generally correspond to the highest  $N_g$  values (Table  
10 5). The minimum  $RF_1$  increases from 70% to 87%, the minimum  $MP_1$  from 71% to 92%, and  
11 the minimum ultimate  $RF$  from 89% to 96%. The maximum  $RF_1$  remains at 96%, the maximum  
12  $MP_1$  increases from 97% to 99%, and the maximum ultimate  $RF$  increases from 96 % to 98%. The  
13 high minimum values observed for a higher depletion level indicate that less favorable geological  
14 scenarios, as classified by high  $N_g$ , can still achieve good performance for UHS.

15 The benefit of higher depletion levels is explained by two key factors. First, a lower initial  
16 amount of  $CH_4$  reduces the amount of impurity that can be produced and increases the volumetric  
17 content of  $H_2$  in the reservoir. By the end of the first cycle injection, on average, 89% of the  
18 reservoir pore volume ( $PV$ ) is occupied by  $H_2$ , compared to 69% in the reference simulations.  
19 Second, lower reservoir pressures (Figure S8) result in smaller density contrasts between  $H_2$  and  
20  $CH_4$ , which mitigates buoyancy forces and thereby reduces gravity override.

21 The lowest  $N_g$  models are less affected by the depletion level than the highest  $N_g$  models  
22 (Figure 8); they have high average performance metrics, above 90%, for both the depletion levels  
23 of 67% and 90%. These models are less sensitive to the initial  $CH_4$  content because their geological  
24 scenarios prevent  $CH_4$  from reaching the well, since their thin sedimentological layers, and sometimes  
25 high dip, mitigate gravity override.

26 The impact of the depletion level on the performance of UHS operations has also been inves-  
27 tigated by Kanaani et al. [23] and Zamehrian and Sedae [49] for a depleted oil reservoir and a  
28 depleted gas condensate reservoir, respectively. Both studies report two competing effects of higher  
29 depletion levels: first, an increased recoverable amount of the formation fluid, which tends to de-  
30 crease  $H_2$  recovery; and second, higher initial reservoir pressures, which are beneficial to  $H_2$  recovery  
31 in their case studies.

32 These competing effects led to complex dependencies of performance on the depletion level. For  
33 example, Zamehrian and Sedae [49] observed an increase in  $RF$  when the depletion level increases  
34 from 30% to 60%; however, the highest tested depletion level of 70% resulted in the lowest  $RF$   
1 because it did not yield sufficient reservoir pressure to produce gas at the target flow rates. This  
2 behavior probably occurs because the minimum BHP was the same in all scenarios; therefore, at  
3 higher depletion levels, part of the injected  $H_2$  in early cycles is trapped for pressure support,  
4 ultimately working as a cushion gas instead of recoverable  $H_2$  [30].



5 In contrast, we reduce the minimum BHP and inject sufficient cushion gas to maintain this  
6 minimum working pressure before the cyclic operation. This comes from the assumption that lower  
7 depletion levels allow for lower minimum BHPs, since these pressures have already been safely  
8 reached before the UHS operations during production of  $\text{CH}_4$ . Because of this assumption, our  
9 model ensemble benefits from the lower amounts of  $\text{CH}_4$  in the reservoir without having the  $\text{H}_2$   
10 deliverability reduced by shorter working pressure ranges.

## 11 4.2 Test 2 — Injected amount of $\text{H}_2$

12 Similarly to the depletion level, decreasing the amount of injected working gas affects mostly the  
13 minimum values of the performance metrics (Figure 7). Compared to the reference simulations,  
14 the minimum  $RF_1$  decreases from 70 % to 68 %, the minimum cycle  $MP_1$  from 71% to 66% and  
15 the minimum ultimate  $RF$  from 89 % to 85%. The maximum values for  $RF_1$  and the ultimate  $RF$   
16 remains largely constant, while the maximum value of  $MP_1$  only increases by 1%.

17 The decrease in the injected mass of  $\text{H}_2$  reduces the proportional amount of  $\text{H}_2$  in the reservoir,  
18 which tends to decrease  $RF$  and purity. By the end of the first cycle injection, on average, 58%  
19 of the reservoir  $PV$  is occupied by  $\text{H}_2$ , against 69% for the reference simulations. The highest  $N_g$   
20 models are more sensitive to this effect. They show an average decrease of 5% in  $RF_1$ , 6% in  $MP_1$   
21 and 3% in the ultimate  $RF$ . In contrast, the lowest  $N_g$  models show a maximum average decrease of  
22 1% in their performance metrics (Figure 8). Therefore, in geologies that intensify gravity override,  
23 operating at high storage capacity is more important. In contrast, geological scenarios where gravity  
24 override is less prevalent can achieve good performance with lower  $\text{H}_2$  injection.

## 25 4.3 Test 3 — No $\text{H}_2$ cushion gas

26 The absence of the  $\text{H}_2$  initialization phase leads to a decrease in performance metrics for the entire  
27 model ensemble (Figure 7). Both the minimum and maximum values of the performance metrics  
28 decrease similarly compared to the reference test. The minimum  $RF_1$  decreases from 70% to  
29 63%, the minimum  $MP_1$  from 71% to 63%, and the minimum ultimate  $RF$  from 90% to 88%.  
30 The maximum  $RF_1$  decreases from 96% to 87%, the maximum  $MP_1$  from 97% to 89%, and the  
31 maximum ultimate  $RF$  from 96% to 94%.

32 The injection of  $\text{H}_2$  cushion gas enhances the purity of the produced gas stream through two  
33 main mechanisms. The first mechanism is the increase in the volumetric content of  $\text{H}_2$  before the  
34 cyclic operations, which ensures a minimum purity during production.  $\text{H}_2$  occupies, on average,  
35 64% of the reservoir  $PV$  by the end of the first cycle injection, compared to 69% in the reference  
36 cases (with cushion gas).

37 The second mechanism through which  $\text{H}_2$  cushion gas enhances purity is by displacing  $\text{CH}_4$   
38 initially in place farther away from the well, which delays its production. The  $\text{H}_2$  cushion gas is  
39 more effective in displacing and segregating  $\text{CH}_4$  in low- $N_g$  models, where it creates stable fronts.  
40 Figures 4 and 5 show, for the reference simulations, the  $\text{H}_2$  plumes after initialization for Model 5  
41 (lowest  $N_g$ ) and Model 12 (highest  $N_g$ ), respectively. The more effective displacement of  $\text{CH}_4$  in  
42 Model 5 results in a later decline in purity and a higher minimum  $FP$  of 89%, compared to 62% for  
1 Model 12 (Figure 9). In the absence of cushion gas, the minimum  $FP$  in Cycle 1 for both models  
2 is similar, around 53%, illustrating how the presence of cushion gas impacts the minimum purity  
3 of the produced gas.

4 The absence of cushion gas causes similar differences in the performance metrics for the lowest



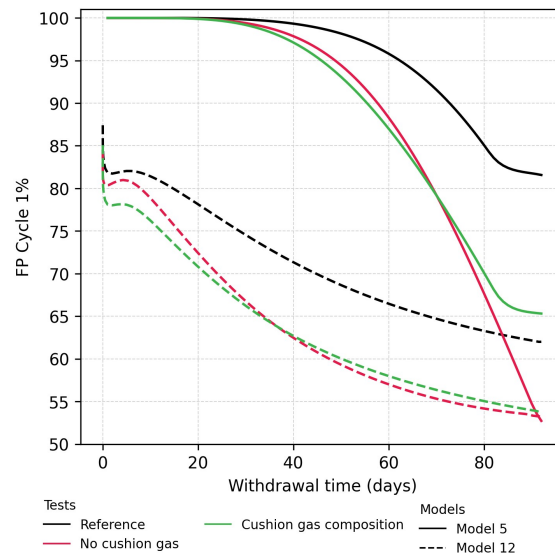


Figure 9: Evolution of the flow purity ( $FP$ ) during the production of cycle 1 in Models 5 and 12 in the reference simulations, Test 3 (No  $H_2$  cushion gas) and Test 4 (Cushion gas composition).

5 and highest  $N_g$  (Figure 8), suggesting that the impact of the amount of cushion gas on UHS  
6 performance is largely insensitive to the geological scenario.

7 In addition to improving purity, the cushion gas can provide pressure support, maintaining the  
8 working pressure above the minimum required BHP. Higher minimum pressures can also reduce  
9 pressure gradients, which limits the lateral spreading of  $H_2$ . However, in our models, pressure  
10 support plays a negligible role because pressure gradients are small [29] and the minimum BHP is  
11 equal to the initial reservoir pressure. The studies that report improvement in UHS performance  
12 due to cushion gas pressure support use models where the minimum BHP is higher than the initial  
13 reservoir pressure, or the reservoirs are large and cannot be uniformly pressurized [e.g. 30, 23].

#### 14 4.4 Test 4 — Cushion gas composition

15 Similar to Test 3, the change in cushion gas composition causes a reduction in the performance  
16 metrics for the entire model ensemble. The minimum  $RF_1$  decreases from 70% to 63%, the minimum  
17  $MP_1$  from 71% to 63% and the minimum ultimate  $RF$  from 89% to 87%. The maximum  $RF_1$   
18 decreases from 96% to 91%, the maximum  $MP_1$  from 97% to 91% and the maximum ultimate  
19  $RF$  from 96% to 95%.

20 The range of performance is similar to that of Test 3 (No cushion gas), indicating that using  
21 a mixture of  $H_2$  and other component as cushion gas may yield no advantage compared to an  
22 operational strategy where there is no cushion gas (Figures 7 and 9). This result is because in our  
1 test with no cushion gas (Test 3), the well deliverability was not affected, due to the assumption of a  
2 lower required minimum BHP. Moreover, the  $CH_4$ - $H_2$  mixture as cushion gas does not significantly  
3 increase the proportion of  $H_2$  in the reservoir. By the end of the first cycle injection,  $H_2$  occupies,  
4 on average, 64% of the  $PV$  when no cushion gas is used (Test 3) and 62% of the  $PV$  when a



5 mixture of  $H_2$  and  $CH_4$  is used as cushion gas.

6 Using a mixture of  $H_2$  and  $CH_4$  as cushion gas can be effective when it results in a significant  
7 increase of the  $H_2$  fraction in the reservoir. It is also useful when pressure support is needed. This  
8 pressure support can also be achieved with cushion gases that do not contain  $H_2$ , at the expense of  
9 a decrease in purity [23].

10 In the case of UHS in aquifers or in gas fields with significant water content, the cushion gas also  
11 plays an important role in displacing water. In this context, the composition of the cushion gas can  
12 further affect the efficiency of this displacement by influencing interfacial tension and wettability  
13 [20], ultimately affecting hydrogen mobility and the strength of capillary trapping.

#### 14 4.5 Test 5 — Well perforation

15 Decreasing the well perforation results in a sharp decrease in the minimum  $RF$ . The minimum  
16  $RF_1$  decreases from 70% to 56%, and the minimum ultimate  $RF$  from 90% to 82%. Conversely,  
17 the minimum  $MP_1$  increases from 71% to 84% (Figure 7).

18 The reduction of the well perforation is one of the only tested strategies that result in poor  
19 correlation between the performance metrics and the  $N_g$ . The highest  $N_g$  models experience  
20 significant performance improvement—on average, increases of 13% in  $RF_1$ , 17% in  $MP_1$ , and 5%  
21 in the ultimate  $RF$  are observed. Meanwhile, the lowest  $N_g$  models experience average decreases  
22 of 3% and 0.5% in  $RF_1$  and the ultimate  $RF$ , respectively, and an average increase of 1% in  $MP_1$ .  
23 As a result, the highest- $N_g$  models show better performance than most of the lowest- $N_g$  models.

24 Nearly all models where  $RF$  decreases have low thickness of layers and high continuity of lacustrine  
25 mudstones in the DOE (Figure 10). Half of the lowest- $N_g$  models share these characteristics  
26 (see Models 5, 7, 29, and 31 in Table A1), explaining their average reduction in  $RF$ . In the model  
27 ensemble by Alshakri et al. [4], models with a high setting for the thickness of layers contain only  
28 one lacustrine mudstone layer at the top of the reservoir, whereas models with low thickness of  
29 layers include several of these mudstones (see Models 5 and 12 in Figure 1).

30 These frequent lacustrine mudstone layers act as baffles that vertically compartmentalize the  
31 reservoir because their permeability can be 4 to 5 orders of magnitude lower than that of the fluvial  
32 sandstones (Table 2). When reducing the well perforation, this compartmentalization causes pressure  
33 discontinuities across the lacustrine mudstones. This results in low average reservoir pressures  
34 and reduction in the performance of UHS. Figure 11 shows that Models 15, 21, 23, and 31, which  
35 exhibit the strongest decreases in cycle  $RF$  (Figure 10), reach lower maximum pressures and higher  
36 minimum pressures compared to the other models.

37 The mechanism of  $H_2$  loss behind the distinct pressure range of these models is illustrated in  
38 Figure 12 for model 31. The vertical reservoir compartments connected to the well experience  
39 higher pressure buildup than the deeper compartments that are not connected to the well. Due  
40 to this vertical pressure gradient,  $H_2$  can reach the deeper compartments, especially through the  
41 channelized sandstones that allow for vertical pressure communication. During the withdrawal of  
42  $H_2$ , the top compartment (connected to the well) reaches the minimum BHP constraint, ceasing  
43 production even though the pressure in the deeper compartments remain above this limit. As  
44 a result of this complex depressurization, some  $H_2$  remains trapped beneath the lower lacustrine  
1 mudstones, leading to low  $RF$ .

2 While this early cessation of production causes a decrease in  $RF$  for the models with low layer  
3 thickness and continuous lacustrine mudstones, it also causes an increase in  $MP$  for most of these  
4 models (Figure 10). This increase occurs because the purity of the produced gas decreases with time



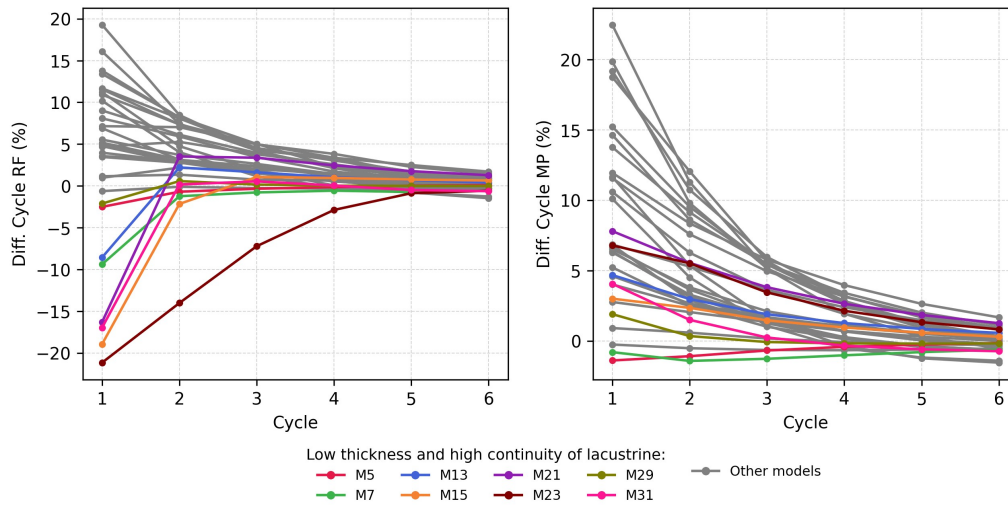


Figure 10: Differences in the cycle recovery factor (left) and mass purity (right) between the reference tests and Test 5 (Well perforation) for the model ensemble. The models with low thickness of the layers and high continuity of the lacustrine mudstone in the DOE are colored. They form a group of models where the initial recovery factor is negatively affected by the reduction in well perforation.

during a cycle production. A sharp decrease of  $FP$  tends to occur in the late stages of production due to  $CH_4$  breakthrough (see, for example, the evolution of  $FP$  for Model 5 in Figure 9. Thus, if the production is stopped early, the minimum  $FP$  increases because  $CH_4$  breakthrough is prevented.

A reduced well perforation is beneficial for the models where the thickness of the reservoir and the sedimentological layers have a high in the DOE, that is, for the highest- $N_g$  models. In these models, the well intersects thick sandstone layers and has no lacustrine mudstone below the perforated interval. For example, Figure 13 shows the evolution of the  $H_2$  plume for Model 12 (which has high  $N_g$ ) during cycle 1. The shorter perforation interval promotes a vertical downwards filling that prevents the occurrence of gravity override. The resulting  $H_2$  plume has an almost horizontal interface with the in-situ  $CH_4$ , forming a  $H_2$  column thicker than the perforated interval. This configuration keeps most of the  $CH_4$  segregated at the bottom of the reservoir, reducing the influx of  $CH_4$  into the well. Note that this behavior is only possible because the injected  $H_2$  volume is large enough to completely fill reservoir along the perforation interval, so the well is mostly hydraulically connected to a region of the reservoir that is filled with  $H_2$ .

The performance metrics for the model ensemble are highly sensitive to the perforation of the well. The reference simulations showed that continuous lacustrine mudstones, i.e the reservoir baffles, enhance UHS performance by mitigating buoyancy forces through compartmentalization [29]. However, if the well perforation does not reach zones below these baffles, they can trap  $H_2$  and reduce  $RF$ . In contrast, the results for models with high with  $N_g$ , i.e. a presumably less favorable geology, show good performance with shorter well perforations. Among the eight highest values of ultimate  $RF$ , seven correspond to models in the highest- $N_g$  set.



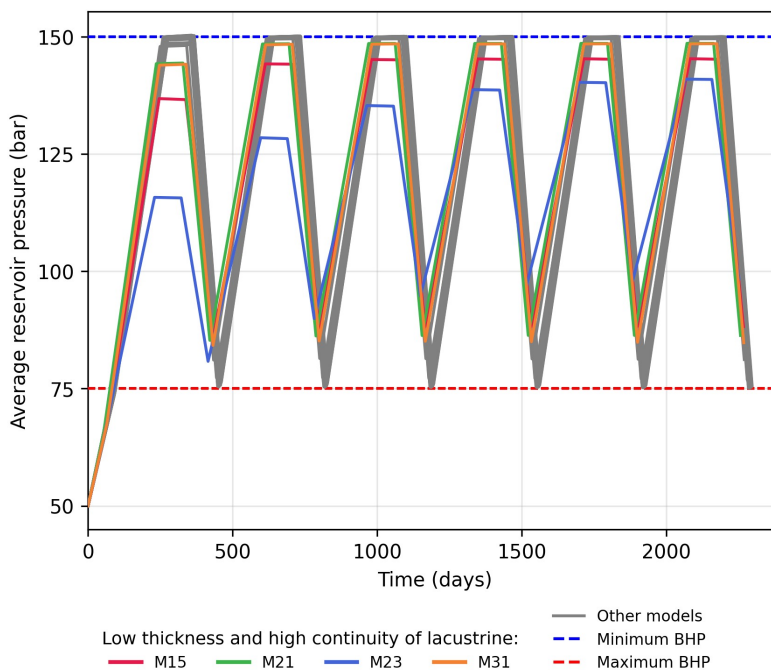


Figure 11: Evolution of the average reservoir pressure during UHS for the entire model ensemble in Test 5 (Well perforation). The models that exhibit the largest decrease in cycle RF are colored.

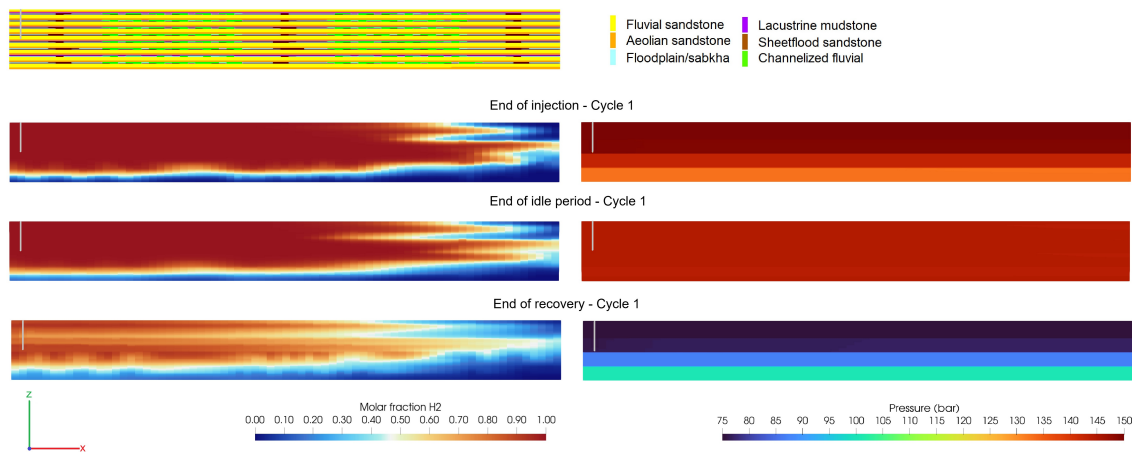


Figure 12: Cross-sectional view of the sedimentological layers, the H<sub>2</sub> plume and the fluid pressures in Model 31 in Test 5 (Well perforation) at different stages of cycle 1. The gray solid line in the models indicates the position of the perforated well.



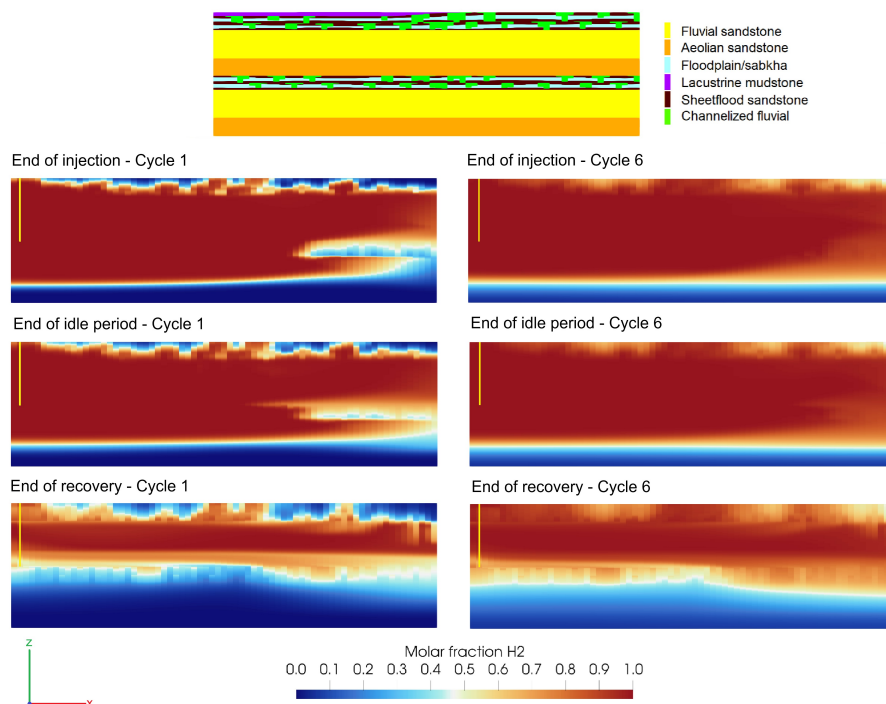


Figure 13: Cross-sectional view of the sedimentological layers and the H<sub>2</sub> plume in Model 12 in Test 5 (Well perforation) at different stages of cycles 1 and 6. The yellow solid line in the models indicates the position of the well perforation.

#### 4.6 Test 6 — Reinjection of co-produced CH<sub>4</sub>

The proposed strategy for the reinjection of co-produced CH<sub>4</sub> (Figure 2) results in significant changes in the performance metrics for the model ensemble. These changes are caused by the combined action of the reinjection of CH<sub>4</sub> in a well perforated at the bottom of the reservoir (CH<sub>4</sub> well) and the reduced perforation of the well used for the injection of H<sub>2</sub> (H<sub>2</sub> well).

Since the impact of the reduced well perforation on UHS performance is already assessed in Test 5 (Well perforation), we take this previous test as a reference for comparison, to isolate the influence of the reinjection of CH<sub>4</sub> on the results. Compared to Test 5, the minimum and maximum *MP* and the minimum *RF*<sub>1</sub> remain approximately the same, but there are significant changes in the other performance metrics (Figure 7). The maximum *RF*<sub>1</sub> increases from 94% to 100%, the minimum ultimate *RF* from 82% to 87% and the maximum ultimate *RF* from 96% to 102%. The maximum values of *RF*<sub>1</sub> and ultimate *RF* above 100% indicate that some of the H<sub>2</sub> initially injected as cushion gas is recovered.

The ultimate *RF* for the lowest and highest *N<sub>g</sub>* models shows average increases (Figure 8) that are largely due to the reinjection of co-produced CH<sub>4</sub>. Compared to the reference simulations, the ultimate *RF* for the lowest *N<sub>g</sub>* models shows an average increase of 6%, against an average decrease of 0.5% when the perforation of the H<sub>2</sub> well is reduced without reinjection of CH<sub>4</sub> (Test 5). The



6 highest  $N_g$  models show an average increase of 9% in the ultimate  $RF$ , against 5% in Test 5.

7 The strategy for the reinjection of co-produced  $\text{CH}_4$  enhances  $RF$  because it repressurizes the  
8 reservoir during production, which helps to maintain the average reservoir pressure above the min-  
9 imum BHP (Figure S8) and prolongs  $\text{H}_2$  deliverability. Moreover, the reinjected  $\text{CH}_4$  replaces part  
10 of the  $\text{H}_2$  cushion gas in its function of maintaining a minimum working pressure. As a conse-  
11 quence, part of the cushion gas can be recovered, leading to a cycle  $RF$  above 100%. In addition  
12 to the pressure support provided by the reinjected  $\text{CH}_4$ , the high values of  $RF$  also result from the  
13 placement of the  $\text{CH}_4$  well at the bottom of the reservoir, which promotes the vertical segregation  
14 of  $\text{H}_2$  and  $\text{CH}_4$  and reduces  $\text{CH}_4$  influx into the  $\text{H}_2$  well.

15 Figure 14 presents the cycle  $RF$  and the difference in cycle  $RF$ , compared to the reference  
16 simulations. For most models, the cycle  $RF$  is always higher than in the reference simulations, and  
17 reaches a value of 100% or higher by cycle 3. As an exception, some models with high continuity  
18 of the lacustrine mudstones and low thickness of layers in the DOE face a pronounced decrease in  
19  $RF_1$ , when compared to the reference simulations (Figure 14). These models require more time for  
20 the pressure support provided by the  $\text{CH}_4$  to become effective, because of the uneven pressurization  
21 caused by the baffles (i.e. the lacustrine mudstones) and the reduced well perforation (Figure 11).  
22 Eventually, these models surpass the cycle  $RF$  of the reference simulations and reach values greater  
23 than 100% for this metric.

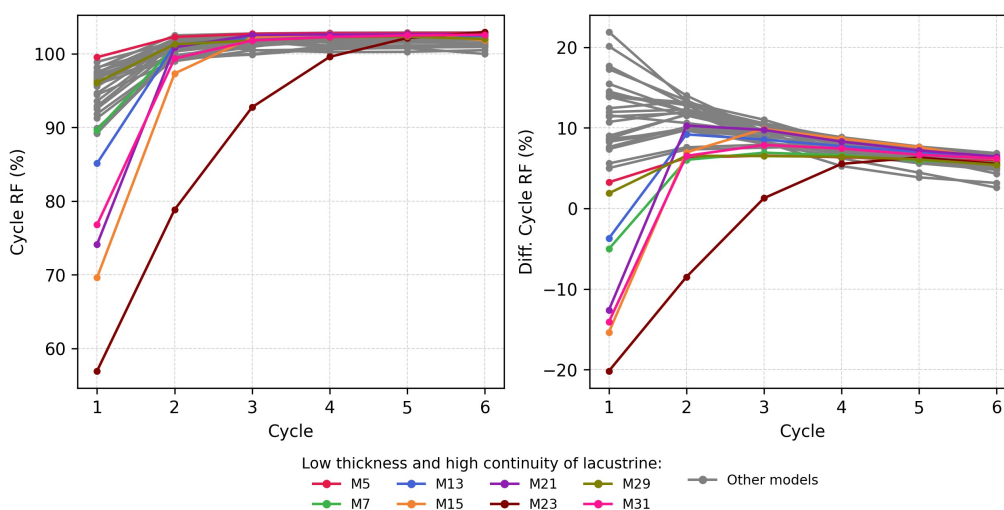


Figure 14: Cycle recovery factor (left) and its difference from the reference tests (right) for Test 6 (Reinjection of co-produced  $\text{CH}_4$ ). The models with low thickness of the layers and high continuity of the lacustrine mudstones in the DOE are colored. They form a set of models whose initial recovery factor is negatively affected by reduced well perforation.

1 Figure 15 presents the cycle  $MP$  and the difference in cycle  $MP$  compared to the reference  
2 simulations. For nearly all models,  $MP$  shows a trend that is significantly different from the  
3 reference simulations and the other operational tests (Figures S1 to S7). In these other simulations,  
4 the cycle  $MP$  increases with increasing cycles due to the replacement of  $\text{CH}_4$  by  $\text{H}_2$  in the reservoir  
5 [29]. But when reinjecting the produced  $\text{CH}_4$ , the cycle  $MP$  remains approximately constant for



6 each model, because the amount of  $\text{CH}_4$  in the reservoir does not decrease.

7 For most of the models in the ensemble,  $MP_1$  is higher when performing the reinjection of  
8 co-produced  $\text{CH}_4$  than in the reference simulations. However, the increase in the cycle  $MP$  tends  
9 to be lost after a few cycles. By cycle 6, the cycle  $MP$  for the entire model ensemble is equal to  
10 or lower than the cycle  $MP$  for the reference simulations, with a difference that can reach -12%  
11 (Figure 15). Thus, the gains in  $RF$  obtained from the reinjection of co-produced  $\text{CH}_4$  come at the  
12 cost of purity in the long-term.

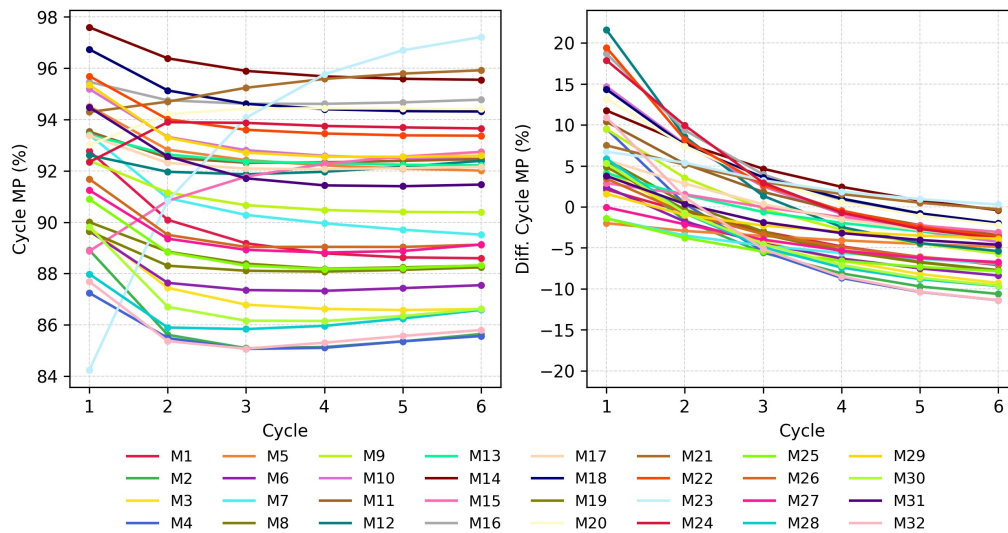


Figure 15: Cycle mass purity (left) and its difference from the reference simulations (right) computed for Test 6 (Reinjection of  $\text{CH}_4$ ).

13 Our models do not prevent the production of the  $\text{H}_2$  cushion gas, part of which becomes unne-  
14 cessary for pressure support once  $\text{CH}_4$  starts to be reinjected. However, the  $\text{H}_2$  cushion gas can also  
15 serve to maintain a minimum purity, as observed when reducing the amount of cushion gas (Test  
16 3) and when changing its composition (Test 4). Thus, alternatively, production can be stopped at  
17 each cycle when  $RF$  reaches 100%.

#### 18 4.7 Test 7 - No idle period

19 The performance metrics for the model ensemble are improved when there is no idle period in the  
20 cyclic operations. Compared to the reference simulations, where the cycles comprise a three-months  
21 idle period, the minimum  $RF_1$  increases by 4%, the minimum  $MP_1$  by 6% and the minimum  
22 ultimate  $RF$  remains stable around 90 %; the maximum  $RF_1$ , maximum  $MP_1$  and maximum  
1 ultimate  $RF$  increase by approximately 1% (Figure 7).

2 During the idle period, mixing by molecular diffusion and buoyancy forces develop without being  
3 counteracted by viscous forces. Although these phenomena contribute to decrease  $RF$  and purity,  
4 the overall influence of the idle period on the performance metrics is considerably smaller than that  
5 of the other tested operational strategies (Figure 8).



6 In our simulations, the dominating physical mechanism during the idle period is gravity segre-  
7 gation promoted by buoyancy forces (Figure 5). Although this phenomenon is intensified during  
8 the idle period, the buoyancy forces are already significant during  $H_2$  injection, as evidenced by the  
9 unstable fronts observed in high  $N_g$  models (Figure 5). Thus, most of the  $H_2$  loss due to gravity  
10 occurs already during the injection, the idle period being a secondary source of loss.

11 Furthermore, the action of buoyancy forces is mostly restricted to initial cycles, when more  $CH_4$   
12 is present in the reservoir. As  $CH_4$  is produced, the importance of these forces decreases. As a  
13 result, the absence of idle periods leads to an increase in the ultimate  $RF$  of only 1%. These results  
14 are consistent with Kanaani et al. [23] and Zamehrian and Sedae [49], who reported small increases  
15 of approximately 1% in the ultimate  $RF$  after suppressing a two-month idle period.

#### 16 4.8 Test 8 - Target rate

17 Among all tested operational strategies, doubling the target rates produced the smallest impact on  
18 the performance metrics (Figure 8). The change in ultimate  $RF$  is small and slightly negative, with  
19 an average decrease of 0.3%. This variation is marginal and likely falls within the numerical error  
20 associated with time stepping and numerical diffusion.

21 Higher injection rates mitigate buoyancy effects by promoting a more viscous-dominated and  
22 less gravity-dominated flow regime. This effect is illustrated in Figure 16, which shows the  $H_2$   
23 plume in Model 12 at the end of the injection of cycle 1. Compared to the reference simulation,  
24 gravity override develops farther from the well. Despite this change in the  $H_2$  plume, doubling the  
25 target rates does not impact  $RF$  for Model 12 significantly, which is representative of the average  
26 behavior of the entire model ensemble.

27 In early cycles, the low impact of the target rates on the performance metrics can be explained  
28 in part by a counter effect that occurs during the idle period. Once the injection is stopped, the  $H_2$   
29 plume rearranges towards a static vertical equilibrium, offsetting the mitigation of gravity override  
30 promoted by higher rates during  $H_2$  injection. For example, the  $H_2$  plume in Model 12 at the end  
31 of the idle period of cycle 1 is similar for the reference simulation and for the simulation where the  
32 target rates are doubled (16). In later cycles, the impact of target rates tends to become even less  
33 significant because the potential loss of  $H_2$  due to gravity override is smaller, since the amount of  
34  $CH_4$  in the reservoir decreases.

35 A second mechanism that counteracts the expected improvement in UHS performance at higher  
36 target rates is the development of stronger pressure gradients along the well. The well intervals  
37 where pressures are lower cease production early, before higher-pressure intervals reach their full  
38 recovery potential. This early cessation of production tends to decrease  $RF$  and also explains the  
39 average increase in  $MP_1$ , as discussed for Test 5 (Well perforation) in Section 4.5.

40 It is important to note that, apart from mitigating gravity override, higher flow rates can also  
41 boost mixing through hydrodynamic dispersion. This latter is not considered in our models, and  
42 could potentially change the impact of higher flow rates on UHS performance.

## 1 5 Guidelines for site screening and field development

2 We observed that the interplay between reservoir geology and operational constraints can impact the  
3 performance of UHS in different ways. We use these observations to establish a general framework  
4 that provides guidelines to identify depleted gas fields that are more suitable for UHS and to plan  
5 operational strategies that optimize UHS operations in these fields.



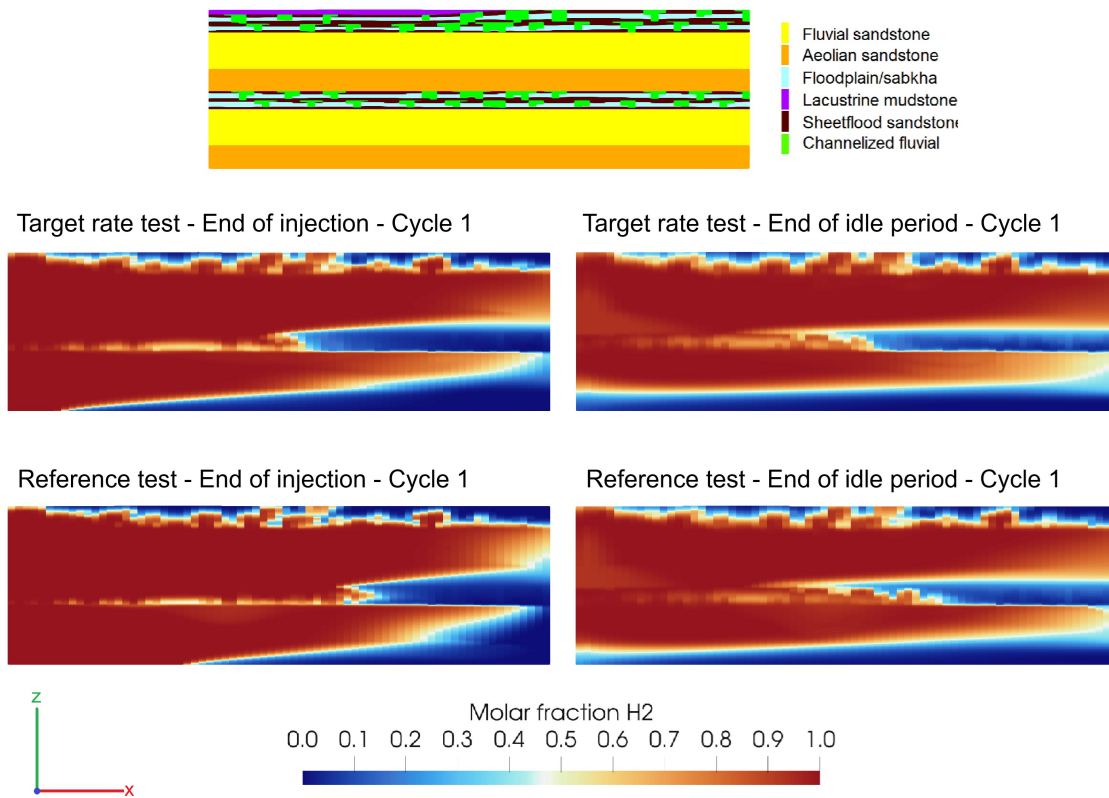


Figure 16: Cross-sectional view of the sedimentological layers and the  $H_2$  plume in Model 12 at the end of the injection and the idle period of cycle 1 for Test 7 (Target rate) and the reference simulations.

6 Figure 17 presents this general framework, which can be divided in guidelines for site screening  
 7 and for development planning. The screening procedure integrates the geological features previously  
 8 identified as key controls, quantified through  $N_g$  in Equation 8, together with two operational  
 9 parameters: depletion level and injected amount of  $H_2$ . The screening is also informed by, and can  
 10 be updated based on, well planning, which therefore sits at the interface between screening and  
 11 development planning.

12 Depletion level, injected amount of  $H_2$ , and well perforation are included in the screening criteria  
 13 because of how they interact with geology. The impact of these strategies on UHS performance  
 14 significantly depends on the reservoir  $N_g$  (Figure 8). Moreover, variations in UHS performance  
 1 due to different well perforations are impacted by the presence of continuous lacustrine mudstones.  
 2 This has important implications because by changing the operational strategies that interact with  
 3 geology, reservoirs with less favorable geology can yield good UHS performance and vice versa.  
 4 Higher depletion levels and a short-enough well perforation yield good UHS performance for geo-  
 5 logical scenarios that have high  $N_g$ , i.e. for reservoirs with less favorable geology. Moreover, the



UHS performance for reservoirs with high  $N_g$  is hindered when the stored amount of  $H_2$  is significantly below full storage capacity, while reservoirs that have low  $N_g$  can perform well for a wider range of depletion levels injected amounts of  $H_2$ . For these reasons, the three operational strategies (depletion level, injected amount of  $H_2$  and well perforation) integrate the screening step.

The framework for development planning includes guidelines for well perforation, which informs and is informed by the screening step, and four operational strategies that do not influence the site selection process: cushion gas amount and composition, reinjection of co-produced formation gas, target rates and the duration of idle periods. These four operational strategies are divided in two categories—low potential and high potential—according to the potential they show in our operational tests to influence UHS performance. The strategies with low potential include the duration of the idle period and the target rates. The strategies with high potential include the amount and composition of the cushion gas and the reinjection of co-produced formation gas ( $CH_4$ ). Despite of their significant influence on UHS performance, these latter strategies can be planned after site screening because they are largely independent from geology. The amount and composition of cushion gas improves UHS performance similarly across all tested geological scenarios (Figure 8). As for the reinjection of co-produced  $CH_4$ , although its impact on UHS performance is highly sensitive to  $N_g$  and to the presence of baffles, this sensitivity arises from the well perforation rather than from the  $CH_4$  reinjection itself.

#### Phase 1: Site screening

#### Phase 2: Development planning of suitable candidates

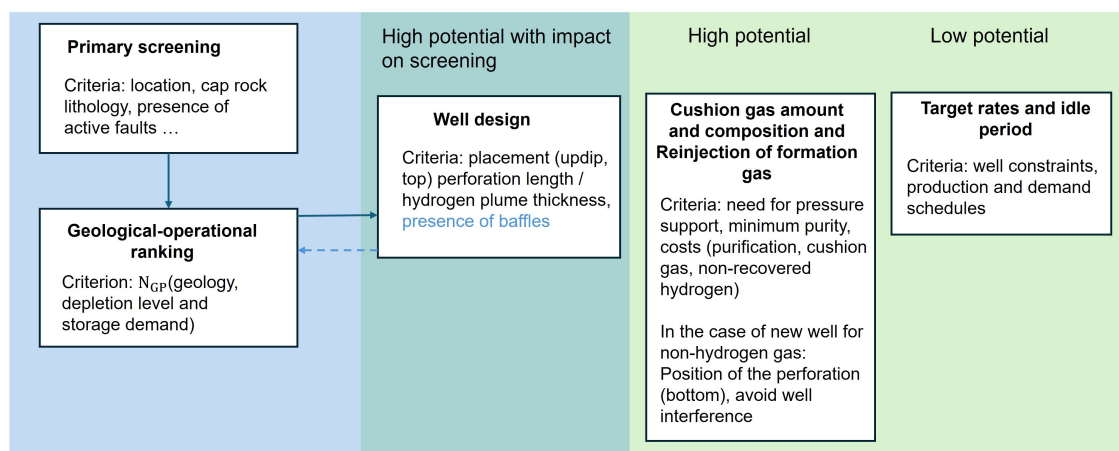


Figure 17: Framework for the site screening (step 1) and development planning (step 2) for UHS in depleted gas fields. The planning of well perforation phase integrates both the screening and the development planning steps.

## 5.1 Criteria and guidelines for site screening

The site-screening step consists of a primary screening followed by a geological–operational screening. The primary screening considers social-technical-economical criteria and characteristics of the reservoir, with the objective of disqualifying reservoirs that can be rapidly judged as unsuitable



6 for UHS. The proposal of these high-level criteria is not the focus of this work. However, several  
7 studies suggest approaches to screen candidate reservoirs for UHS worldwide, commonly consider-  
8 ing criteria such as the proximity of the site to renewable-energy installations, cities, and pipeline  
9 networks [40, 17], as well as the lithology of the caprock [22, 35, 27, 11] and the presence of faults  
10 [35, 27, 11].

11 The main novelty proposed here is the the geological-operational approach to further screen and  
12 rank candidates that are qualified in the primary screening. This approach provides a method to  
13 rank and select the depleted gas fields building on the analysis presented here and our earlier work  
14 [29]. This geological-operational screening should be viewed as a step within a broader screening  
15 procedure, and does not preclude the addition of further screening steps based on physical phe-  
16 nomena that are not accounted for in our models, such as H<sub>2</sub> loss due to biogeochemical reactions  
17 [44, 11]; multiphase displacement effects governed by wettability, interfacial tension, and residual  
18 trapping [47, 15]; and leakage through the caprock, bounding faults, and abandoned wells [47, 16].

19 Candidate reservoirs for UHS have different geological scenarios, depletion levels, and storage  
20 capacities. The interaction that was observed between geology (characterized by the reservoir  
21  $N_g$ ), depletion level and stored amount of H<sub>2</sub> implies that they must be considered together for  
22 site screening. Depletion level and stored mass of H<sub>2</sub> ultimately modify the relative proportions  
23 of H<sub>2</sub> and CH<sub>4</sub> in the reservoir. The strength of buoyancy forces, given by  $N_g$ , determines the  
24 susceptibility of the reservoir to producing CH<sub>4</sub> due to gravity override; but the amount of CH<sub>4</sub>  
25 that actually is produced depends on the fluid composition in the reservoir i.e. the proportional  
26 amount of CH<sub>4</sub> and H<sub>2</sub>.

27 Figures 18a and 18b illustrate this concept. They depict scenarios in which different volumes  
28 of H<sub>2</sub> are injected into two reservoirs with identical geology and identical rock and fluid properties.  
29 Because buoyancy forces depend only on these properties, their magnitude is the same in both  
30 reservoirs. The limiting state for the action of buoyancy forces is the hydrostatic equilibrium shown  
31 in the figures, where a column of H<sub>2</sub> develops over a column of denser formation gas, which here  
32 is CH<sub>4</sub>. The volumes occupied by these columns in the reservoir depend on the proportional mass  
33 of injected H<sub>2</sub> and CH<sub>4</sub>, and have implications for the composition of the gas produced at the well.  
34 The reservoir with the lower injected volume of H<sub>2</sub> contains a higher proportional amount of CH<sub>4</sub>;  
35 as a result, it leads to a lower minimum purity under the same buoyancy forces than in the other  
36 reservoir.

37 Based on this concept, we propose scaling the buoyancy-force component of the modified gravity  
38 number (Equation 8) with the mass ratio of CH<sub>4</sub> and H<sub>2</sub> to define the Gravity–Purity Number, given  
39 by:

$$N_{GP} = F_b \frac{M_{CH_4}}{M_{H_2}} = k_x H g \Delta \rho \cos \alpha \frac{M_{CH_4}}{M_{H_2}}, \quad (9)$$

40 where  $F_b$  is buoyancy force,  $k_x$  is the reservoir upscaled longitudinal permeability,  $H$  is the thickness  
41 of the depositional cycle (repeating sandstone–mudstone patterns),  $\alpha$  is the reservoir dip angle,  $g$   
42 is gravitational acceleration,  $\Delta \rho$  is the density difference between H<sub>2</sub> and CH<sub>4</sub>,  $M_{CH_4}$  is the mass  
1 of CH<sub>4</sub> initially in place, and  $M_{H_2}$  is the maximum stored mass of H<sub>2</sub>. The density difference  $\Delta \rho$   
2 should be computed at a consistent reference pressure and temperature for all reservoirs. Here, we  
3 computed the fluid densities at the minimum BHP, following Loyola et al. [29], and at the constant  
4 reservoir temperature of 55°C. The mass  $M_{H_2}$  is the maximum stored mass of H<sub>2</sub> in one cycle. The  
5 mass  $M_{CH_4}$  is computed as:

$$M_{CH_4} = V_r \bar{\phi} \rho_{CH_4}(T_0, p_0), \quad (10)$$



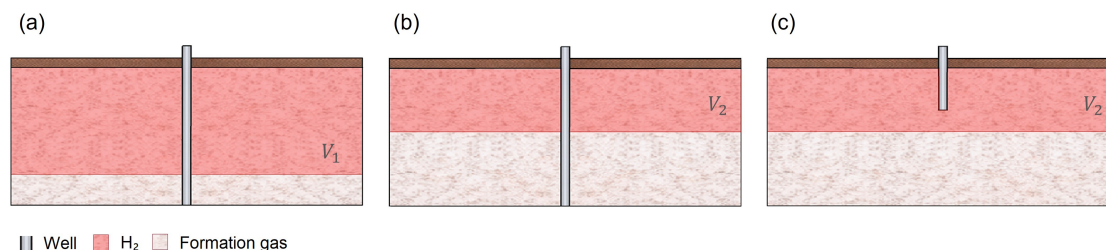


Figure 18: Conceptual models for the configuration of  $H_2$  and a denser formation gas after the full development of buoyancy forces in identical reservoirs, considering two injected volumes of  $H_2$  ( $V_1$  and  $V_2$ , with  $V_1 > V_2$ ) and two well perforations. The reservoirs in (a) and (b) have the same well perforation but different injected amounts of  $H_2$ . As a result, the minimum purity of the produced  $H_2$  is lower in reservoir (b). The reservoir in (c) has the lowest injected amount of  $H_2$  but a shorter well perforation than the others; as a result, it recovers  $H_2$  at a higher purity than reservoir (b), despite having the same injected  $H_2$  volume.

6 where  $V_r$  and  $\bar{\phi}$  are the reservoir volume and average porosity, respectively, and  $\rho_{CH_4}(T, p_0)$  is the  
7 density of  $CH_4$  as computed for the initial reservoir pressure ( $p_0$ ) and temperature ( $T_0$ ).

8 Note that  $N_{GPF}$  is not dimensionless, unlike  $N_g$ . It has units of force, as it scales the magnitude  
9 of buoyancy forces with the  $H_2$ - $CH_4$  mass ratio to express their potential impact on purity and  
10 recovery factor. We omit the viscous-force component of the gravity number, because flow rates  
11 were observed to have limited impact on UHS performance; therefore, they are considered only in  
12 later stages of the development planning step (Figure 17).

13 Figure 19 shows that, when considering the reference tests together with Test 1 (Depletion level)  
14 and Test 2 (Injected amount),  $N_{GPF}$  correlates strongly with the ultimate  $RF$ . For this reason, we  
15 propose  $N_{GPF}$  as the main criterion in the geological-operational screening.  $N_{GPF}$  allows the ranking  
16 of storage units using geological features (e.g. reservoir thickness, dip, and upscaled permeability),  
17 depletion level, and store mass of  $H_2$ . By incorporating operational strategies,  $N_{GPF}$  improves the  
18 modified  $N_g$  with the consideration of operational strategies that control the mass proportion of  
19  $H_2$  in the reservoir.

20 Figure 19 illustrates that  $N_{GPF}$  captures the high improvement in UHS performance for highest  
21  $N_g$  models when the depletion level is high. It also shows that the lowest  $N_g$  models achieve ultimate  
22  $RF$  values above 91% regardless of the tested depletion level or injected  $H_2$ . Thus, models with  
23 low  $N_g$  imply good UHS performance in situations where depletion level and storage volumes are  
24 uncertain.

25  $N_{GPF}$  assigns a higher ranking to a candidate field as the depletion level increases. This is  
26 a direct consequence of the assumption made in our operational tests, according to which the  
27 deliverability of  $H_2$  at the well is not compromised by lower reservoir pressures and BHPs. It is  
1 possible, nonetheless, that target production rates require a minimum BHP that is well above the  
2 pressure of the depleted gas field. In that case, the proposed site screening can be further enhanced  
3 by disqualifying reservoirs with pressures significantly lower than the desired minimum working  
4 pressure. The estimation of a minimum working pressure for the well system should be feasible  
5 during site selection, because target rates are dictated by a previously identified  $H_2$  demand that



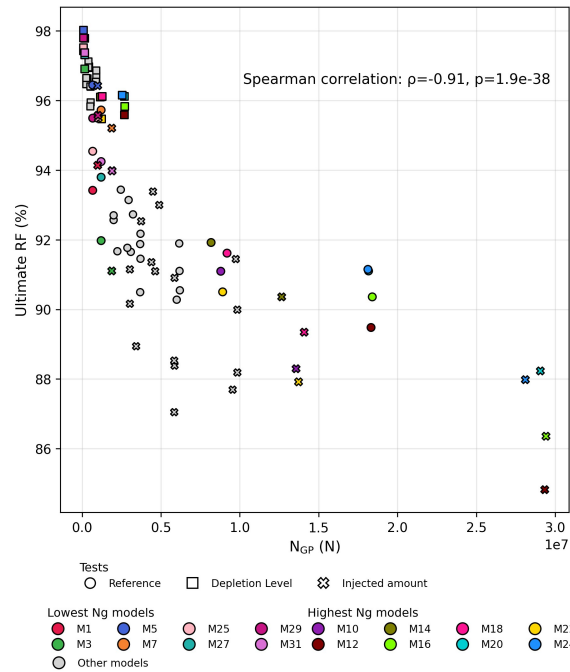


Figure 19: Correlation between the gravity–purity number ( $N_{GP}$ ) and the ultimate recovery factor ( $RF$ ) for the entire model ensemble in the reference simulations, Test 1 (Depletion level), and Test 2 (Injected amount of  $H_2$ ). The lowest- $N_g$  and highest- $N_g$  models are highlighted. Different operational tests are represented by different symbols.

6 justifies the UHS operation. This disqualification represents one way in which well planning can  
 7 influence the site selection process. Nonetheless, providing criteria for this disqualification is out  
 8 of the scope of the current work, since it would require consideration of the design of wellbore  
 9 hydraulics and surface facilities.

## 10 5.2 Criteria and guidelines for development planning

11 The framework for development planning provides guidelines to design different operational strate-  
 12 gies for UHS. These strategies are categorized according to their low or high potential to optimize  
 13 UHS performance.

14 We propose the types of criteria that can be used to design operational strategies, without  
 15 defining precise quantitative values or detailing specific evaluation methods. The purpose of this  
 1 framework is to provide guidelines that serve as starting points for more detailed, interdisciplinary  
 2 and site-specific assessments of UHS operational strategies.

### 3 5.2.1 Well perforation

4 A sufficiently short well perforation can mitigate gravity override in geological scenarios with high  
 5  $N_g$ . Figure 17 presents the criteria to optimize well perforation. If a depleted reservoir contains



6 multiple wells, these criteria can also be used to identify the most suitable wells to be repurposed  
7 for injecting  $H_2$ .

8 The well should be placed updip, and be perforated the top of the reservoir, since the  $H_2$  tends  
9 to migrate upwards due to gravity segregation from the formation gas. In addition, perforation  
10 length is a key factor controlling UHS performance (see Section 4.5). If the injected volume of  $H_2$   
11 is large enough to fill the reservoir to a thickness greater than the well perforation, the formation  
12 gas is displaced downward away from the well (Figure 13 and Figure 18c). Hence, we propose that  
13 the well perforation should be short enough to be hydraulically connected only to reservoir zones  
14 that are filled with  $H_2$ . This recommendation is particularly relevant for reservoirs with higher  
15  $N_g$ , which are more susceptible to buoyancy forces.

16 Figures 18b and 18c provide conceptual models illustrating the interplay between the well per-  
17 foration and the injected amount of  $H_2$ . If the well perforation is short relative to the thickness  
18 occupied by the  $H_2$  column, inflow to the well will consist predominantly of  $H_2$  (Figure 18c). Oth-  
19 erwise, the well will also be hydraulically connected to deeper zones occupied by formation gas  
20 (Figure 18b).

21 The presence of laterally continuous baffles is also a critical factor to consider when planning  
22 well perforation. In our model ensemble, the baffles are laterally continuous mudstones that have  
23 maximum permeability of 0.01 mD, which is 4 to 5 orders of magnitude smaller than the permeabil-  
24 ity of the fluvial sandstones. These baffles compartmentalize the reservoir and reduce the effective  
25 thickness over which buoyancy forces act, thereby mitigating gravity override and potentially im-  
26 proving UHS performance [29]. However, they also pose a risk of trapping  $H_2$  in geobodies below  
27 them that are not connected to the well. Therefore, if laterally extensive baffles are present in the  
28 reservoir, the well perforation should be long enough to reach zones below the baffles to which  $H_2$   
29 can migrate.

30 In practice, there is often significant uncertainty regarding the lateral extent of baffles inter-  
31 secting wells. If a reservoir contains frequent baffles of uncertain extent, the risk of  $H_2$  trapping  
32 beneath them exists. This risk can be mitigated by perforating the well across the entire reservoir  
33 thickness. When this strategy is not feasible, the most conservative approach do deal with this  
34 uncertainty is to disqualify such reservoirs for UHS. In this way, well-perforation planning informs  
35 and updates the screening stage.

36 While the criteria for well perforation planning are based on numerical models involving a single  
37 well for  $H_2$  injection and production, these criteria can be applied individually to each well when  
38 multiple wells are used, taking into account their respective zones of influence within the reservoir.

39 We restrict ourselves to providing criteria for well perforation, which directly interacts with  
40 reservoir geology and is considered in our tests. However, as stated in Section 5.1, other aspects of  
41 well design, notably working pressure constraints, could also inform the site screening process.

## 42 5.2.2 Cushion gas and reinjection of formation gas strategy

43 The cushion gas amount and composition have high potential to improve UHS performance. These  
44 strategies should be defined based on at least three criteria: the need for pressure support, the  
1 required minimum purity, and total costs.

2 Pressure support is required when the reservoir pressure is lower than the minimum working  
3 pressure. It can also be used to improve  $H_2$  production when the reservoir is expected to develop  
4 high pressure gradients during storage operations, which favor the migration of hydrogen away from  
5 the well. The required minimum purity depends on the intended application for the  $H_2$ . The use of



6 cushion gas can improve the purity of the H<sub>2</sub> produced at the well, potentially reducing purification  
7 costs.

8 The cushion gas composition is particularly relevant for meeting purity requirements. While  
9 pressure support can be provided by any type of gas, improvements in the minimum purity of the  
10 produced H<sub>2</sub> are achieved mainly through the use of H<sub>2</sub>-containing cushion gas.

11 All these considerations need to be evaluated together with a cost assessment. Ultimately, a  
12 cushion gas strategy is only effective if the costs associated with the cushion gas are compensated  
13 by gains in H<sub>2</sub> production or by reductions in purification costs.

14 The reinjection of co-produced formation gas is a waste management solution that can also  
15 provide pressure support to the reservoir. Similar to the planning of the cushion gas strategy, this  
16 strategy requires consideration of the need for pressure support, as well as careful evaluation of  
17 minimum purity requirements and costs. The reinjection of co-produced formation gas tends to  
18 maintain the purity of the produced H<sub>2</sub> at approximately constant levels and to increase purification  
19 costs in the long term (see Section 4.6). Moreover, this strategy requires an additional injection well.  
20 To limit the co-production of formation gas after reinjection, this well should be perforated near the  
21 bottom of the reservoir and should not have pressure interference with the H<sub>2</sub> injection–production  
22 well. The same considerations apply if a separate well is planned for injecting any cushion gas other  
23 than H<sub>2</sub>.

### 24 5.2.3 Idle period duration and target rates

25 The duration of the idle period and the target rates should be adjusted to factors external to  
26 the reservoir, such as expected schedules for H<sub>2</sub> production and energy demand. The planning of  
27 target rates should also consider the constraints of the injection system and the well. Since these  
28 parameters are influenced by external factors, they are not flexibly adjustable. Moreover, since  
29 they depend on H<sub>2</sub> production demand, they are expected to vary. The limited flexibility in their  
30 adjustment and their variability are not detrimental to the operation and should not interfere with  
31 the site selection process, as both operational strategies showed low impact on UHS performance  
32 metrics and limited interaction with geology in our operational tests.

## 33 6 Conclusions

34 We performed several operational tests, corresponding to simulations of UHS with different opera-  
35 tional strategies, using a model ensemble that contains various geological scenarios for the Bunter  
36 sandstone. The tested operational strategies include depletion level, injected amount of hydrogen,  
37 cushion gas amount and composition, well perforation, reinjection of co-produced gas, duration of  
38 the idle period and target rates.

39 The operational tests are based on a set of reference simulations, based on which we identified  
40 the geological controls on UHS performance and proposed a modified gravity number as a geological  
41 screening criterion. We identified the potential impact of the tested strategies on UHS performance  
1 by comparing the results of the operational tests with those of the reference simulations. We also  
2 assessed the interaction between operational strategies and reservoir geology by comparing how the  
3 strategies affected UHS performance metrics across different geological scenarios, mainly relying on  
4 comparisons between reservoir models with low and high gravity numbers. The main findings of  
5 the operational tests are summarized below.



- 6 • UHS performance in reservoirs with high gravity numbers is sensitive to the depletion level and  
7 can be adequate if the depletion level is high. On the other side, reservoirs with low gravity  
8 number can achieve strong UHS performance at a higher range of depletion levels because  
9 they are less susceptible to gravity override. This conclusion is based on the assumption that  
10 lower minimum working pressures can be used for higher depletion levels without affecting  
11 well deliverability.
- 12 • UHS performance in reservoirs with high gravity numbers is also sensitive to the injected  
13 amount of hydrogen. In these reservoirs, operating below storage capacity compromises per-  
14 formance. In contrast, reservoirs with lower gravity numbers perform well across the tested  
15 injected masses of hydrogen.
- 16 • Changes in the amount and composition of cushion gas cause significant differences on UHS  
17 performance metrics that are largely independent of geology.
- 18 • UHS performance in reservoirs with high gravity numbers can be significantly improved if the  
19 well perforation is sufficiently short and placed at the top of the reservoir. The perforation  
20 length should be short enough to be hydraulically connected to reservoir zones filled mostly  
21 with hydrogen.
- 22 • If the reservoir has frequent and laterally continuous baffles, there is a risk of hydrogen  
23 trapping. In these cases, the well perforation should be long enough to reach the geobodies  
24 below the baffles, where hydrogen may be trapped.
- 25 • The reinjection of produced formation gas is a waste management solution that also serves to  
26 provide pressure support to the reservoir. This strategy can improve the recovery factor at  
27 the cost of a long-term reduction in purity.
- 28 • The duration of the idle period and the target rates have low potential to affect UHS per-  
29 formance.

30 In summary, reservoirs with high gravity number can be engineered to yield good UHS per-  
31 formance if critical operational strategies such as well perforation and depletion level are carefully  
32 planned. Reservoirs with low gravity numbers offer more flexibility for different operational strate-  
33 gies and are therefore better-suited to handle operational uncertainties.

34 Based on these findings, we proposed a framework for site screening and development planning  
35 for UHS in depleted gas fields. The site screening framework includes a screening criterion called the  
36 gravity–purity number, an extension of our modified gravity number that integrates geological and  
37 operational aspects. This criterion can be used to select candidate gas reservoirs that minimize the  
38 loss of hydrogen through buoyancy effects, considering their geology and the proportional amount  
39 of hydrogen and resident gas in the reservoir. This latter depends on operational parameters such  
40 as depletion level and the stored volume of hydrogen. The screening step is also informed by  
41 the identification of laterally extensive baffles in the reservoir, which pose the risk of trapping of  
42 hydrogen.

1 The gas reservoirs identified as suitable for UHS by the screening procedure should undergo  
2 more detailed studies as part of their development planning, which includes the design of the well  
3 system and the choice of cushion gas. Our proposed framework indicates the types of criteria that  
4 should guide the optimisation of these strategies. These criteria are often external to the reservoir  
5 — typically related to cost analysis and well-system constraints — so development planning is



6 inevitably interdisciplinary. We do not provide objective criteria for these external factors, which  
7 should be addressed in complementary studies to the reservoir geology and engineering analyses  
8 presented here. The selection of optimal UHS strategies for target fields requires an integrated  
9 approach combining techno-economic analyses with coupled reservoir–wellbore flow simulations.

10 The physical phenomena considered in the numerical models are isothermal gas flow and molecu-  
11 lar diffusion. The main source of hydrogen loss in this setting is gravity override; thus, the proposed  
12 guidelines for screening and development planning target the mitigation of undesired gravity effects.  
13 However, other physical processes that may cause hydrogen loss, such as hydrogen-consuming reac-  
14 tions, dispersion, water flow due to aquifer support, capillary effects and other interfacial phenom-  
15 ena, were not included. Future studies should incorporate these physical phenomena and evaluate  
16 their impact on hydrogen loss to refine the screening and development planning framework.

## 17 Acknowledgments

18 The authors thanks Shell Global Solutions International B.V. for sponsoring this work through  
19 ASSET program and granting permission to publish this work. The authors also thank the Shell  
20 hydrogen team for discussions and feedback during the project. Sebastian Geiger thanks Energi  
21 Simulation for supporting his Chair in Sustainable Geoenergy.

## 22 References

- 23 [1] Northern lights project. <https://norlights.com/>. Accessed in November 2025.
- 24 [2] Porthos project. <https://www.porthosco2.nl/en/project/>. Accessed in November 2025.
- 25 [3] International Energy Agency. Global hydrogen review 2025. pages 139–142, 2025.
- 26 [4] Jafar Alshakri, Gary J. Hampson, Carl Jacquemyn, Matthew D. Jackson, Dmytro Petrovskyy,  
27 Sebastian Geiger, Julio D.Machado Silva, Sicilia Judice, Fazilatur Rahman, and Mario Costa  
28 Sousa. A screening assessment of the impact of sedimentological heterogeneity on co2 migration  
29 and stratigraphic-baffling potential: Sherwood and bunter sandstones, uk. *Geological Society*  
30 *Special Publication*, 528:245–266, 2023. doi: 10.1144/SP528-2022-34.
- 31 [5] Zhenkai Bo, Maartje Boon, Hadi Hajibeygi, and Suzanne Hurter. Impact of experimentally  
32 measured relative permeability hysteresis on reservoir-scale performance of underground hy-  
33 drogen storage (UHS). *International Journal of Hydrogen Energy*, 48:13527–13542, 4 2023.  
34 doi: 10.1016/j.ijhydene.2022.12.270.
- 35 [6] Toni Busch, Jonas Derichs, Theresa Klütz, Jochen Linßen, and Detlef Stolten. The hydro-  
36 gen supply chain — a comprehensive literature review incorporating purity analysis. *In-*  
1 *ternational Journal of Hydrogen Energy*, 164:149367, 2025. ISSN 0360-3199. doi: <https://doi.org/10.1016/j.ijhydene.2025.04.532>. URL [https://www.sciencedirect.com/science/](https://www.sciencedirect.com/science/article/pii/S036031992502244X)  
2 [article/pii/S036031992502244X](https://www.sciencedirect.com/science/article/pii/S036031992502244X).  
3
- 4 [7] Hans Cleijne, Mats de Ronde, Martijn Duvoort, Willem de Kleuver, and Jillis Raadschelders.  
5 North sea energy outlook, 2020.



- 6 [8] Delft High Performance Computing Centre (DHPC). DelftBlue Supercomputer (Phase 2).  
7 <https://www.tudelft.nl/dhpc/ark:/44463/DelftBluePhase2>, 2024.
- 8 [9] Department of Energy and Climate Change. UK renewable energy roadmap, 2011.
- 9 [10] Nikolaos Diamantakis, Anna Peacock, Omid Shahrokhi, Sudhagar Pitchaimuthu, and John M.  
10 Andresen. A review of analogue case studies relevant to large-scale underground hydro-  
11 gen storage. *Energy Reports*, 11:2374–2400, 2024. ISSN 2352-4847. doi: [https://doi.org/](https://doi.org/10.1016/j.egyr.2024.02.002)  
12 [10.1016/j.egyr.2024.02.002](https://doi.org/10.1016/j.egyr.2024.02.002). URL [https://www.sciencedirect.com/science/article/pii/](https://www.sciencedirect.com/science/article/pii/S2352484724000878)  
13 [S2352484724000878](https://www.sciencedirect.com/science/article/pii/S2352484724000878).
- 14 [11] Nikolaos Diamantakis, Anna Peacock, Omid Shahrokhi, Sudhagar Pitchaimuthu, and John M.  
15 Andresen. A review of analogue case studies relevant to large-scale underground hydrogen  
16 storage. *Energy Reports*, 11:2374–2400, 6 2024. doi: [10.1016/j.egyr.2024.02.002](https://doi.org/10.1016/j.egyr.2024.02.002).
- 17 [12] Cecchetti Emilio, Martinius Allard W., Bruna Pierre-Olivier, Bender Annelies, and  
18 Abels Hemmo A. Structural controls on the triassic main buntsandstein sediment distribution  
19 in the roer valley graben, the netherlands. *Netherlands Journal of Geosciences*, 103, Nov.  
20 2024. doi: [10.1017/njg.2024.17](https://doi.org/10.1017/njg.2024.17). URL [https://njpgjournal.nl/index.php/njpg/article/](https://njpgjournal.nl/index.php/njpg/article/view/11622)  
21 [view/11622](https://njpgjournal.nl/index.php/njpg/article/view/11622).
- 22 [13] Reza Ershadnia, Mrityunjay Singh, Saeed Mahmoodpour, Alireza Meyal, Farzad Moieni,  
23 Seyyed Abolfazl Hosseini, Daniel Murray Sturmer, Mojdeh Rasoulzadeh, Zhenxue Dai, and  
24 Mohamad Reza Soltanian. Impact of geological and operational conditions on underground  
25 hydrogen storage. *International Journal of Hydrogen Energy*, 48:1450–1471, 1 2023. doi:  
26 [10.1016/j.ijhydene.2022.09.208](https://doi.org/10.1016/j.ijhydene.2022.09.208).
- 27 [14] Nicolas Foote, Stuart J. Hatter, Ewan Gray, and Dimitrios Charlaftis. Reservoir charac-  
28 terization of the triassic bunter sandstone in the 43/28-nepbh1 borehole: implications for  
29 co2 storage in the neighbouring endurance structure, southern north sea, uk. *Geoenergy*, 3  
30 (1):geoenergy2025–012, 10 2025. ISSN 2755-1725. doi: [10.1144/geoenergy2025-012](https://doi.org/10.1144/geoenergy2025-012). URL  
31 <https://doi.org/10.1144/geoenergy2025-012>.
- 32 [15] Ianna Gomez Mendez, Waleed M. M. El-Sayed, Anne H. Menefee, and Zuleima T. Karpyn.  
33 Insights into underground hydrogen storage challenges: A review on hydrodynamic and bio-  
34 geochemical experiments in porous media. *Energy & Fuels*, 38(21):20015–20032, 2024. doi:  
35 [10.1021/acs.energyfuels.4c03142](https://doi.org/10.1021/acs.energyfuels.4c03142).
- 36 [16] Ruichang Guo, Hongsheng Wang, Jianqiao Leng, and Seyyed A. Hosseini. Evaluation of hy-  
37 drogen leakage through abandoned wells to overlaying saline aquifers during underground  
38 hydrogen storage in depleted natural gas reservoirs. *Gas Science and Engineering*, 140:  
39 205659, 2025. ISSN 2949-9089. doi: <https://doi.org/10.1016/j.jgsce.2025.205659>. URL  
1 <https://www.sciencedirect.com/science/article/pii/S2949908925001232>.
- 2 [17] Saeed Harati, Sina Rezaei Gomari, Manu Ramegowda, and Tannaz Pak. Multi-criteria site  
3 selection workflow for geological storage of hydrogen in depleted gas fields: A case for the uk.  
4 *International Journal of Hydrogen Energy*, 51:143–157, 2024. ISSN 0360-3199. doi: [https://](https://doi.org/10.1016/j.ijhydene.2023.10.345)  
5 [doi.org/10.1016/j.ijhydene.2023.10.345](https://doi.org/10.1016/j.ijhydene.2023.10.345).



- 6 [18] Aliakbar Hassanpouryouzband, Edris Joonaki, Katriona Edlmann, Niklas Heinemann, and  
7 Jinhai Yang. Thermodynamic and transport properties of hydrogen containing streams. *Sci-*  
8 *entific Data*, 7:222, 2020. doi: 10.1038/s41597-020-0568-6. URL <https://doi.org/10.1038/s41597-020-0568-6>.
- 10 [19] Aliakbar Hassanpouryouzband, Edris Joonaki, Katriona Edlmann, and R. Stuart Haszeldine.  
11 Offshore geological storage of hydrogen: Is this our best option to achieve net-zero?, 2021.  
12 ISSN 23808195.
- 13 [20] Zoha Dalal Isfehiani, Amirmansour Jafari, Jalal Fahimpour, Mirhasan Hosseini, Stefan Iglauer,  
14 and Alireza Keshavarz. Sandstone wettability and mixed gas composition: Unraveling the  
15 impact of co2 in hydrogen geo-storage. *International Journal of Hydrogen Energy*, 59:1352–  
16 1366, 2024. ISSN 0360-3199. doi: <https://doi.org/10.1016/j.ijhydene.2024.02.120>. URL <https://www.sciencedirect.com/science/article/pii/S0360319924005354>.
- 18 [21] Carl Jacquemyn, Margaret E. H. Pataki, Gary J. Hampson, Matthew D. Jackson, Dmytro  
19 Petrovskyy, Sebastian Geiger, Clarissa C. Marques, Julio D. Machado Silva, Sicilia Judice,  
20 Fazilatur Rahman, and Mario Costa Sousa. Sketch-based interface and modelling of stratigra-  
21 phy and structure in three dimensions. *Journal of the Geological Society*, 178(4):jgs2020–187,  
22 03 2021. ISSN 0016-7649. doi: 10.1144/jgs2020-187.
- 23 [22] Joaquim Juez-Larré, Serge van Gessel, Rory Dalman, Gijs Remmelts, and Remco Groenberg.  
24 Assessment of underground energy storage potential to support the energy transition in the  
25 netherlands. *First Break*, 37(7):57–66, 2019. ISSN 1365-2397. doi: <https://doi.org/10.3997/1365-2397.n0039>.
- 27 [23] Mahdi Kanaani, Behnam Sedae, and Mojtaba Asadian-Pakfar. Role of cushion gas on under-  
28 ground hydrogen storage in depleted oil reservoirs. *Journal of Energy Storage*, 45, 1 2022. doi:  
29 10.1016/j.est.2021.103783.
- 30 [24] Mark Khait and Denis Voskov. Adaptive parameterization for solving of thermal/compositional  
31 nonlinear flow and transport with buoyancy. *SPE Journal*, 23(2):522 – 534, 2018. doi: 10.  
32 2118/182685-pa.
- 33 [25] Sam Kobeissi, Nicholas N.A. Ling, Kaishuo Yang, Eric F. May, and Michael L. Johns. Dis-  
34 persion of hydrogen in different potential cushion gases. *International Journal of Hydrogen*  
35 *Energy*, 60:940–948, 3 2024. doi: 10.1016/j.ijhydene.2024.02.151.
- 36 [26] S. Korevaar, R. Dalman, S. Nelskamp, S. Atkins, E. Boter, E. Wiarda, M. Nolten, and K. Bein-  
37 tema. Play 5 triassic. <https://www.geodeatlas.nl/pages/play-5-triassic>, 2023. Ac-  
38 cessed: 04 07, 2025.
- 39 [27] Leszek Lankof, Katarzyna Luboń, Yann Le Gallo, and Radosław Tarkowski. The ranking of  
40 geological structures in deep aquifers of the polish lowlands for underground hydrogen storage.  
1 *International Journal of Hydrogen Energy*, 62:1089–1102, 4 2024. doi: 10.1016/j.ijhydene.2024.  
2 03.106.
- 3 [28] Eric W. Lemmon, Ian H. Bell, Marcia L. Huber, and Mark O. McLinden. Thermophysical  
4 properties of fluid systems. NIST Chemistry WebBook, NIST Standard Reference Database  
5 Number 69, 2025. Retrieved April 10, 2025.



- 6 [29] Ana Loyola, Denis Voskov, Rouhi Farajzadeh, Kevin Bisdom, Karin de Borst, and Sebastian  
7 Geiger. Geological controls on underground hydrogen storage in depleted gas fields. *Journal*  
8 *of Energy Storage*, 2025.
- 9 [30] Maksim Lysyy, Martin Fernø, and Geir Ersland. Seasonal hydrogen storage in a depleted  
10 oil and gas field. *International Journal of Hydrogen Energy*, 46:25160–25174, 7 2021. doi:  
11 10.1016/j.ijhydene.2021.05.030.
- 12 [31] Xiacong Lyu and Denis Voskov. Advanced modeling of enhanced co2 dissolution trapping in  
13 saline aquifers. *International Journal of Greenhouse Gas Control*, 127, 2023. doi: 10.1016/j.  
14 ijggc.2023.103907.
- 15 [32] Xiacong Lyu, Mark Khait, and Denis Voskov. Operator-based linearization approach for  
16 modeling of multiphase flow with buoyancy and capillarity. *SPE Journal*, 26(4):1858 – 1878,  
17 2021. doi: 10.2118/205378-PA.
- 18 [33] Giacomo Medici, L. West, and Nigel Mountney. Sedimentary flow heterogeneities in the Triassic  
19 U.K. Sherwood sandstone group: Insights for hydrocarbon exploration. *Geological Journal*, 54,  
20 05 2018. doi: 10.1002/gj.3233.
- 21 [34] Netherlands Oil and Gas Portal (NLOG). Temperature data. [https://www.nlog.nl/en/  
22 temperature-data](https://www.nlog.nl/en/temperature-data). Accessed in August 2025.
- 23 [35] Esuru Rita Okoroafor, Sarah D. Saltzer, and Anthony R. Kavscek. Toward underground  
24 hydrogen storage in porous media: Reservoir engineering insights. *International Journal of*  
25 *Hydrogen Energy*, 47:33781–33802, 9 2022. ISSN 03603199. doi: 10.1016/j.ijhydene.2022.07.  
26 239.
- 27 [36] D. W. Peaceman. Interpretation of well-block pressures in numerical reservoir simulation.  
28 *Society of Petroleum Engineers Journal*, 18(3):183–194, 1978. doi: 10.2118/6893-PA. SPE-  
29 6893-PA.
- 30 [37] D. Petrovskyy, C. Jacquemyn, S. Geiger, M. D. Jackson, G. J. Hampson, J. D. Machado Silva,  
31 S. Judice, F. Rahman, and M. Costa Sousa. Rapid flow diagnostics for prototyping of reservoir  
32 concepts and models for subsurface co2 storage. *International Journal of Greenhouse Gas*  
33 *Control*, 124, 3 2023. doi: 10.1016/j.ijggc.2023.103855.
- 34 [38] W. T. Pfeiffer, S. A. al Hagrey, D. Köhn, W. Rabbel, and S. Bauer. Porous media hy-  
35 drogen storage at a synthetic, heterogeneous field site: numerical simulation of storage  
36 operation and geophysical monitoring. *Environmental Earth Sciences*, 75, 8 2016. doi:  
37 10.1007/s12665-016-5958-x.
- 38 [39] Rawaa A. Sadkhan and Watheq J. Al-Mudhafar. Key aspects of underground hydrogen  
39 storage in depleted hydrocarbon reservoirs and saline aquifers: A review and understand-  
1 ing. *Energy Geoscience*, 5(4):100339, 2024. ISSN 2666-7592. doi: [https://doi.org/10.  
2 1016/j.engeos.2024.100339](https://doi.org/10.1016/j.engeos.2024.100339). URL [https://www.sciencedirect.com/science/article/pii/  
3 S2666759224000544](https://www.sciencedirect.com/science/article/pii/S2666759224000544).
- 4 [40] Alireza Safari, Yuichi Sugai, Mohammad Sarmadivaleh, and Motonao Imai. Screening and  
5 ranking japanese gas fields for underground h2 storage potential: Impact of the reservoir



- 6 drive mechanism. *Journal of Energy Storage*, 70:107679, 2023. ISSN 2352-152X. doi: <https://doi.org/10.1016/j.est.2023.107679>.
- 7
- 8 [41] A. Sainz-Garcia, E. Abarca, V. Rubi, and F. Grandia. Assessment of feasible strategies for  
9 seasonal underground hydrogen storage in a saline aquifer. *International Journal of Hydrogen*  
10 *Energy*, 42:16657–16666, 6 2017. doi: 10.1016/j.ijhydene.2017.05.076.
- 11 [42] Mike Shook, Dachang Li, and Larry Lake. Scaling immiscible flow through permeable media  
12 by inspectional analysis. *In Situ-NY*, 16:4:311–349, 01 1992.
- 13 [43] Radoslaw Tarkowski. Underground hydrogen storage: Characteristics and prospects. *Renew-*  
14 *able and Sustainable Energy Reviews*, 105:86–94, 5 2019. doi: 10.1016/j.rser.2019.01.051.
- 15 [44] Eike M. Thaysen, Sean McMahon, Gion J. Strobel, Ian B. Butler, Bryne T. Ngwenya, Niklas  
16 Heinemann, Mark Wilkinson, Aliakbar Hassanpouryouzband, Christopher I. McDermott, and  
17 Katriona Edlmann. Estimating microbial growth and hydrogen consumption in hydrogen  
18 storage in porous media. *Renewable and Sustainable Energy Reviews*, 151:111481, 2021. ISSN  
19 1364-0321. doi: <https://doi.org/10.1016/j.rser.2021.111481>.
- 20 [45] Mariska M. van Eijk. Volpriehausen prospectivity review. *MSc thesis, VU University Amster-*  
21 *dam*, 2014.
- 22 [46] B. M. M. van Kempen, H. F. Mijnlief, and J. van der Molen. Data mining in the dutch oil and  
23 gas portal: a case study on the reservoir properties of the volpriehausen sandstone interval.  
24 *Geological Society, London, Special Publications*, 469:253–267, 2018. doi: 10.1144/SP469.1.
- 25 [47] Willemijn A. van Rooijen and Hadi Hajibeygi. Site selection for underground hydrogen storage  
26 in porous media: Critical review and outlook. *Energy & Fuels*, 39(41):19600–19613, 2025. doi:  
27 10.1021/acs.energyfuels.5c03665.
- 28 [48] Denis Voskov, Ilshat Saifullin, Aleks Novikov, Michiel Wapperom, Luisa Orozco, Gabriel Serrão  
29 Seabra, Yuan Chen, Mark Khait, Xiaocong Lyu, Xiaoming Tian, Stephan De Hoop, and  
30 Artur Palha. open Delft Advanced Research Terra Simulator(open-DARTS). 9(99):6737,  
31 2024. ISSN 2475-9066. doi: 10.21105/joss.06737. URL [https://joss.theoj.org/papers/](https://joss.theoj.org/papers/10.21105/joss.06737)  
32 [10.21105/joss.06737](https://joss.theoj.org/papers/10.21105/joss.06737).
- 33 [49] Mohammad Zamehrian and Behnam Sedaee. Underground hydrogen storage in a partially  
34 depleted gas condensate reservoir: Influence of cushion gas. *Journal of Petroleum Science and*  
1 *Engineering*, 212, 5 2022. doi: 10.1016/j.petrol.2022.110304.
- 1108 [50] Lingping Zeng, Regina Sander, Yongqiang Chen, and Quan Xie. Hydrogen storage performance  
1109 during underground hydrogen storage in depleted gas reservoirs: A review. *Engineering*, 40:  
1110 211–225, 2024. ISSN 2095-8099. doi: <https://doi.org/10.1016/j.eng.2024.03.011>. URL <https://www.sciencedirect.com/science/article/pii/S2095809924002285>.  
1111



1112 **A Design of Experiment**

Table A1: DOE composed of 32 different combinations of the factors A to J in Table 1, where L stands for low setting and H for high setting.

	Models 1-16										Models 17-32										
	A	B	C	D	E	F	G	H	I	J	A	B	C	D	E	F	G	H	I	J	
1	L	L	L	L	H	L	L	L	L	L	17	L	L	L	L	L	H	L	L	H	H
2	H	L	L	L	H	L	H	H	L	L	18	H	L	L	L	L	H	H	H	H	H
3	L	H	L	L	L	L	H	H	L	L	19	L	H	L	L	H	H	H	H	H	H
4	H	H	L	L	L	L	L	L	L	L	20	H	H	L	L	H	H	L	L	H	H
5	L	L	H	L	L	L	L	H	L	H	21	L	L	H	L	H	H	L	H	H	L
6	H	L	H	L	L	L	H	L	L	H	22	H	L	H	L	H	H	H	L	H	L
7	L	H	H	L	H	L	H	L	L	H	23	L	H	H	L	L	H	H	L	H	L
8	H	H	H	L	H	L	L	H	L	H	24	H	H	H	L	L	H	L	H	H	L
9	L	L	L	H	L	L	H	L	H	L	25	L	L	L	H	H	H	H	L	L	H
10	H	L	L	H	L	L	L	H	H	L	26	H	L	L	H	H	H	L	H	L	H
11	L	H	L	H	H	L	L	H	H	L	27	L	H	L	H	L	H	L	H	L	H
12	H	H	L	H	H	L	H	L	H	L	28	H	H	L	H	L	H	H	L	L	H
13	L	L	H	H	H	L	H	H	H	H	29	L	L	H	H	L	H	H	H	L	L
14	H	L	H	H	H	L	L	L	H	H	30	H	L	H	H	L	H	L	L	L	L
15	L	H	H	H	L	L	L	L	H	H	31	L	H	H	H	H	H	L	L	L	L
16	H	H	H	H	L	L	H	H	H	H	32	H	H	H	H	H	H	H	L	L	L

Open Access Article. Published on 25 June 2026. Downloaded on 6/26/2026 1:22:11 PM.  
This article is licensed under a Creative Commons Attribution 3.0 Unported Licence.



Environmental Science: Advances Accepted Manuscript

## Data Availability Statement

View Article Online  
DOI: 10.1039/D6VA00162A

The numerical simulations performed in this study use a completely open-source framework, based on open-DARTS, Rapid Reservoir Modeling (RRM), and the ensemble of open-access geological models for the Bunter sandstone designed by Alshakri et al. (2022). Open-DARTS is available at: <https://gitlab.com/open-darts/open-darts>; RRM is available at: <https://bitbucket.org/rapidreservoirmodelling/rrm>; and the Bunter geological models are available at: [https://figshare.com/articles/dataset/RRM\\_models\\_of\\_Sherwood\\_and\\_Bunter\\_Sandstones/19210002](https://figshare.com/articles/dataset/RRM_models_of_Sherwood_and_Bunter_Sandstones/19210002). Moreover, the open-DARTS models for the reference simulations of this study are also available at: <https://zenodo.org/records/19442719>. Note that these models are compatible with version 1.2.1 of open-DARTS.

